Long-wavelength surface-tension-driven Bénard convection: experiment and theory

By STEPHEN J. VANHOOK, MICHAEL F. SCHATZ†,
J. B. SWIFT, W. D. McCORMICK,
AND HARRY L. SWINNEY

Center for Nonlinear Dynamics and Department of Physics,
University of Texas at Austin, Austin, TX 78712, USA
e-mail: svanhook@chaos.ph.utexas.edu

Surface-tension-driven Bénard (Marangoni) convection in liquid layers heated from below can exhibit a long-wavelength primary instability that differs from the more familiar hexagonal instability associated with Bénard. This long-wavelength instability is predicted to be significant in microgravity and for thin liquid layers. The instability is studied experimentally in terrestrial gravity for silicone oil layers 0.007 to 0.027 cm thick on a conducting plate. For shallow liquid depths (< 0.017 cm for 0.102 $cm^2 s^{-1}$ viscosity liquid), the system evolves to a strongly deformed long-wavelength state which can take the form of a localized depression ('dry spot') or a localized elevation ('high spot'), depending on the thickness and thermal conductivity of the gas layer above the liquid. For slightly thicker liquid depths (0.017–0.024 cm), the formation of a dry spot induces the formation of hexagons. For even thicker liquid depths (> 0.024 cm), the system forms only the hexagonal convection cells. A two-layer nonlinear theory is developed to account properly for the effect of deformation on the interface temperature profile. Experimental results for the long-wavelength instability are compared to our two-layer theory and to a one-layer theory that accounts for the upper gas layer solely with a heat transfer coefficient. The two-layer model better describes the onset of instability and also predicts the formation of localized elevations, which the one-layer model does not predict. A weakly nonlinear analysis shows that the bifurcation is subcritical. Solving for steady states of the system shows that the subcritical pitchfork bifurcation curve never turns over to a stable branch. Numerical simulations also predict a subcritical instability and yield long-wavelength states that qualitatively agree with the experiments. The observations agree with the onset prediction of the two-layer model, except for very thin liquid layers; this deviation from theory may arise from small non-uniformities in the experiment. Theoretical analysis shows that a small non-uniformity in heating produces a large steady-state deformation (seen in the experiment) that becomes more pronounced with increasing temperature difference across the liquid. This steady-state deformation becomes unstable to the long-wavelength instability at a smaller temperature difference than that at which the undeformed state becomes unstable in the absence of non-uniformity.

---

† Present address: School of Physics, Georgia Institute of Technology, Atlanta, GA 30332, USA.

1. Introduction

Surface-tension-driven phenomena are important not only for their influence on the fundamental physics of interfacial flows, but also for their potential industrial applications, particularly in microgravity where buoyancy effects nearly disappear. In the presence of temperature variations on a liquid–fluid interface, the temperature dependence of surface tension ($\mathrm{d}\sigma/\mathrm{d}T \equiv -\sigma_T < 0$) causes cool regions of the interface to pull liquid from warm regions of the interface. This thermocapillary mechanism can drive fluid flow and lead to instabilities in non-isothermal free-surface systems (Davis 1987). In surface-tension-driven Bénard convection (henceforth called 'Marangoni convection'), a liquid layer is heated from below and cooled from above (see figure 1). In thin liquid layers or in microgravity, the buoyancy mechanism of Rayleigh–Bénard convection becomes negligible, leaving thermocapillarity as the dominant driving mechanism (Davis & Homsy 1980).

Bénard (1900) performed some of the earliest studies of convection in liquid layers almost a century ago. Heating thin layers (≈ 1 mm deep) of spermaceti from below, he found a transition from conduction to polygonal (quasi-hexagonal) convection cells of wavenumber $q \equiv 2\pi d/\lambda \approx 2$, where d is the mean liquid depth and λ is the wavelength of the cells. Block (1956) and Pearson (1958) first recognized that surface tension, not buoyancy, was the source of the instability. Bénard's experiments have been repeated (Koschmieder & Biggerstaff 1986) and the most recent experiment by Schatz *et al.* (1995) found onset of the instability in close agreement with the prediction of linear stability analysis (Pearson 1958; Nield 1964). In addition, Schatz *et al.* found that the bifurcation was subcritical with 3.2% hysteresis, larger than predicted by nonlinear theory (Scanlon & Segel 1967, 2.3%; Cloot & Lebon 1984, 0.2%).

A second and completely different instability due to surface tension also exists in this same system and should become primary in very thin or very viscous liquid layers or in microgravity. This long-wavelength ($q = 0$) deformational mode was first predicted thirty years ago by Scriven & Sternling (1964) and Smith (1966) and has recently been observed experimentally by VanHook *et al.* (1995). In the experiments, a thin liquid layer heated from below became unstable and eventually formed a large-scale drained region ('dry spot'). The experiments found onset of the instability to occur 35% below the prediction of linear stability analysis of a one-layer model (Takashima 1981*a*; Goussis & Kelly 1990; Pérez-García & Carneiro 1991; Wilson 1993).

Another long-wavelength instability, unrelated to the one described in the previous paragraph, was predicted by Pearson (1958) and further discussed by Sivashinsky (1982), Garcia-Ybarra, Castillo & Velarde (1987), and Hadji, Safar, & Schell (1991) for perfectly insulating top and bottom boundaries. Since this instability is predicted to occur for even a non-deformable interface, it is fundamentally different from the long-wavelength instability that is the subject of this paper. Pantaloni *et al.* (1979) claimed to observe the long-wavelength mode of Pearson in silicone oil on top of a glass plate; however, it is clear they did not observe this state because the bottom boundary condition was conducting relative to the liquid ($k_{glass}/k \approx 6$). Takashima (1970) generalized Pearson's analysis to finite k_{bottom}/k and predicted little difference between the case of an infinitely conducting bottom and $k_{bottom}/k = 6$; in addition, for k_{bottom}/k even as small as 0.1, he predicts a finite wavelength ($q \approx 1$). Observation of the long-wavelength mode with insulating boundaries would require $k_{bottom}/k < 0.01$ and $d/d_g \ll 1$. Even styrofoam has too large a thermal conductivity by an order of magnitude.
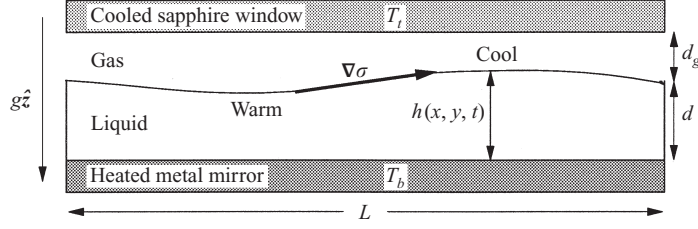
FIGURE 1. Sketch of a surface-tension-driven Bénard (Marangoni) convection cell of horizontal extent L, mean liquid depth d, mean gas depth d_g, and local interface position $h(x, y, t)$. In all experiments $L/d > 100$, and d_g is typically twice d. The sapphire window is cooled to temperature T_t and the mirror is heated to temperature T_b. Since surface tension decreases with increased temperature, temperature variations generate surface tension gradients, which can initiate fluid flow.

Parameter	Symbol	Value at 50 °C
Surface tension	σ	19 dyn cm^{-1}
Surface-tension coefficient	σ_T	0.069 dyn cm^{-1} K^{-1}
Liquid density	ρ	0.94 g cm^{-3}
Liquid thermal diffusivity	κ	0.001 cm^2 s^{-1}
Liquid kinematic viscosity	v	0.102 cm^2 s^{-1}
Liquid thermal expansion	α	0.001 °C^{-1}
Liquid thermal conductivity	k	13.3×10^3 erg s^{-1} cm^{-1} K^{-1}
Gas thermal conductivity	k_g	2.76×10^3 erg s^{-1} cm^{-1} K^{-1} (air)
		15.3×10^3 erg s^{-1} cm^{-1} K^{-1} (He)

TABLE 1. Fluid parameter values

The hexagonal and long-wavelength instabilities differ in the stabilizing mechanisms that compete with destabilizing thermocapillary effects due to different types of fluctuations. The short-wavelength hexagonal instability originates from temperature fluctuations on the free surface, which initiate thermocapillary flow along the interface; the imposed vertical temperature difference across the liquid layer sustains the flow. Thermal and viscous diffusion, however, dampen the temperature fluctuations and associated fluid flow. Alternatively, the long-wavelength mode originates from fluctuations of the free-surface height $h(x, y)$, which cause a temperature variation on the interface because of the imposed temperature gradient. By thermocapillarity, the cool elevated region pulls liquid from the warm depressed region and, if allowed to continue, thermocapillarity would pile all the liquid from one region of the layer into an adjacent region. Gravity, though, attempts to flatten the interface and thus to stabilize these deformational perturbations. In addition, surface tension selects a long wavelength for this deformational instability since surface tension resists *curvature* of the interface and thus stabilizes long-wavelength modes least.

The onset behaviour of the system is determined by three time scales – thermocapillary ($t_{therm}^2 = \rho d^3 / \sigma_T \Delta T$), gravitational ($t_{grav}^2 = d/g$), and diffusive ($t_{diff}^2 = d^4 / v \kappa$), where g is the gravitational acceleration, ΔT is a characteristic temperature difference across the liquid layer, and other parameters are defined in figure 1 and table 1. Thermocapillarity is destabilizing, while gravity and diffusion are stabilizing. The Galileo number,

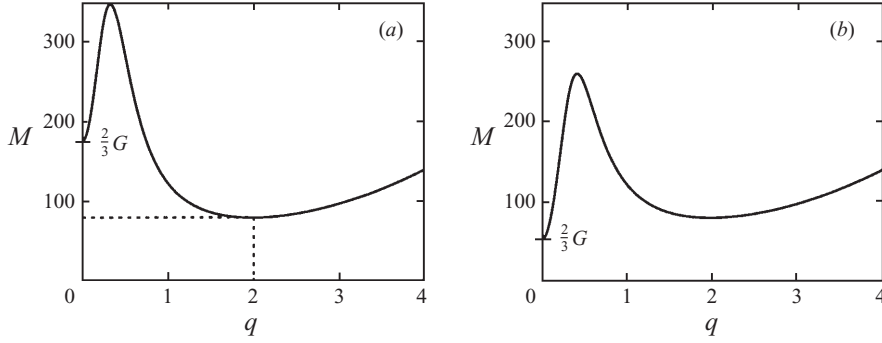$$G \equiv \frac{t_{diff}^2}{t_{grav}^2} = \frac{g d^3}{v \kappa}, \tag{1.1}$$

FIGURE 2. Marginal stability curves for $v = 0.10$ cm^2 s^{-1} silicone oil in terrestrial gravity according to linear stability theory for $d/d_g \ll 1$ (see, for example, Smith 1966). (a) For $d = 0.03$ cm, the primary instability appears at $M = 80$ with $q = 1.99$. (b) For $d = 0.02$ cm, the minimum at $q = 0$ becomes the global minimum and the primary instability occurs at $q = 0$ and $M = 2G/3 = 52$.

determines which instability will appear – the stabilizing mechanism with the longest time scale (i.e. the slowest-acting stabilizing mechanism) determines the criterion for onset.

When G is sufficiently large, the response time of gravity is short enough that deformational perturbations are quickly stabilized. The liquid surface can be considered effectively flat and the formation of short-wavelength (hexagonal) convection cells due to temperature perturbations is the primary instability (see figure 2a). The relevant parameter for determining stability in this case is the Marangoni number, or

$$M \equiv \frac{t_{diff}^2}{t_{therm}^2} = \frac{\sigma_T \Delta T d}{\rho \nu \kappa}. \tag{1.2}$$

When $M > 80$ (Pearson 1958), thermocapillarity is strong enough to overcome diffusion and onset of short-wavelength convection occurs.

When G is small, the diffusive time scale is very short, temperature perturbations are quickly damped, and gravity is relatively weak so that deformational perturbations which generate the long-wavelength instability are slowly stabilized. The long-wavelength instability becomes primary (see figure 2b) and the relevant parameter for determining onset of the instability is the inverse dynamic Bond number,

$$D \equiv \frac{t_{grav}^2}{t_{therm}^2} = \frac{M}{G} = \frac{\sigma_T \Delta T}{\rho g d^2}. \tag{1.3}$$

When $D > \approx 2/3$ (Smith 1966), the thermocapillary effect is strong enough to overcome gravity and the system is unstable to long-wavelength deformations.

When both liquid and gas layers are conducting and the interface is not deformed, the uniform temperature difference across the liquid layer ΔT can be calculated from the top T_t and bottom T_b temperatures,

$$\Delta T = \frac{T_b - T_t}{1 + d_g k/dk_g} = \frac{(T_b - T_t)H}{1 + H}, \tag{1.4}$$

where $H = dk_g/d_g k$. The long-wavelength instability is a deformational mode, however, and in the presence of deformation the temperature field is no longer horizontally uniform. For small deformation, the mean temperature difference across the layer $\langle \Delta T \rangle$ is still given by (1.4). For large deformation, however, (1.4) does

Dimensionless number	Symbol	Definition	Typical values
Galileo	G	$gd^3/\nu\kappa$	0–150
Marangoni	M	$\sigma_T \Delta T d/\rho\nu\kappa$	0–100
Inverse dynamic bond	D	$\sigma_T \Delta T/\rho g d^2$	0–0.7
Rayleigh	R	$\alpha g \Delta T d^3/\nu\kappa$	0–1
Static Bond	B	$\rho g (L/2\pi)^2/\sigma$	18
Biot	H	$k_g d/k d_g$	0–1
Two-layer Biot	F	$(d/d_g - H)/(1 + H)$	−0.1–1.0
Crispation	Cr	$\rho\nu\kappa/\sigma d$	10^{-4}–10^{-3}
Prandtl	Pr	ν/κ	100

TABLE 2. Dimensionless quantities and experimental values

not give $\langle \Delta T \rangle$ (see §4); the difference between ΔT as defined in (1.4) and $\langle \Delta T \rangle$ is model-dependent, but for either the one- or two-layer models, ΔT differs from $\langle \Delta T \rangle$ by only a few percent for moderate deformation. Using $\langle \Delta T \rangle$ as the characteristic temperature drop across the liquid is problematic since then D would increase when the instability occurs and the interface begins to deform, even for fixed T_b and T_t. We use ΔT as defined by (1.4) as the characteristic temperature difference across the liquid for both theory and experiment; thus there is no problem in comparing experiment to theory.

Marangoni convection has been described by both one-layer and two-layer models. One-layer models explicitly model the liquid layer and model the upper gas layer solely with a heat transfer coeffiecient (the Biot number). Two-layer models explicitly model both liquid and gas layers. In this paper, we employ a two-layer model that takes into account the conduction heat transfer in the gas layer in the presence of deformation, but ignores convection in the gas layer.

Section 2 discusses the one-layer model which has been employed in most theoretical work on the Marangoni problem. Section 3 begins by explaining the necessity of using a two-layer model for the long-wavelength instability and the remainder of §3 develops a two-layer nonlinear theory for the long-wavelength mode. Section 3.1 derives a nonlinear evolution equation to describe the instability; §3.2 performs a linear analysis of the evolution equation; §3.3 performs a weakly nonlinear analysis to determine the nature of the bifurcation; §3.4 solves for steady states for a one-dimensional interface (rolls); §3.5 discusses numerical simulations of the evolution equation. Section 3.6 discusses the effect of non-uniformity in the system. Section 4 describes the experimental design and §5 presents the experimental results. Conclusions are given in §6.

2. One-layer model

Most linear stability analyses of the Marangoni problem (Pearson 1958; Nield 1964; Takashima 1981a; Goussis & Kelly 1990; Pérez-García & Carneiro 1991; Wilson 1993) have employed a one-layer model, where the effect of the gas in the upper layer is modelled solely by a heat transfer coefficient, the Biot number, which for a flat interface is

$$H(q) = q \frac{k_g}{k} \coth q \frac{d_g}{d} \qquad (2.1)$$

(see, for example, equation 8.91 of Cross & Hohenberg 1993 or the appendix of Hadji *et al.* 1991). As $q \to 0$, $H \to k_g d / k d_g$ (for the remainder of the paper, H will mean $H(q \to 0)$). The earliest linear stability analyses assumed a non-deformable interface (Pearson 1958; Nield 1964) and thus never discovered the inherently deformational long-wavelength mode. Scriven & Sternling (1964) first predicted this long-wavelength instability, which they found marginally stable at $M = 0$. Thus, according to their analysis, this $q = 0$ mode should always appear before the hexagons and, in fact, appear with infinitesimal ΔT. Smith (1966) pointed out that their analysis ignored gravity, which induces hydrostatic pressure differences that resist deformation. Depending on the strength of gravity, either the hexagonal or the long-wavelength mode could appear as the primary instability. Later linear stability analyses employing a one-layer model that allowed for deformation (Takashima 1981*a*; Goussis & Kelly 1990; Pérez-García & Carneiro 1991) predicted onset of the $q = 0$ mode at

$$D_c = \tfrac{2}{3}(1 + H). \tag{2.2}$$

These results are for an infinite system. A finite system of horizontal extent L has a lowest-order mode of $q = 2\pi d / L$, which should become unstable at a slightly higher ($\sim O(q^2)$) value of D.

While the one-layer linear stability theory successfully predicts the onset of the $q = 1.99$ Pearson/Bénard instability, it is less successful with the long-wavelength instability. The only experiment to test this theory (VanHook *et al.* 1995) found that the onset in the experiments occurs 35% earlier than predicted by the one-layer linear theory.

A one-layer model nonlinear evolution equation for the long-wavelength instability was derived by Davis (1983) for $H = 0$. A slightly different equation was derived by Funada (1987), and the extension to finite H was derived by Kopbosynov & Pukhnachev (1986) and Oron & Rosenau (1992). A linear stability analysis based on this equation agrees with (2.2). Numerical simulations of the equation find the formation of a large-scale dry spot (Joo, Davis & Bankoff 1991; VanHook *et al.* 1995; Krishnamoorthy & Ramaswamy 1995), in qualitative accord with what is seen in experiments (VanHook *et al.* 1995).

3. Two-layer model

A thermocapillary model with two fluid layers was first considered by Smith (1966). He found a negligible correction (of order 1% for most parameters) to the one-layer prediction for the onset of hexagons ($q = 2$), but found onset of the long-wavelength mode ($q = 0$) at

$$D_c = \frac{2(1 + H)}{3(1 + d / d_g)} = \frac{2}{3(1 + F)} \tag{3.1}$$

(equation (28) in his paper), where the new parameter, which we call the two-layer Biot number,

$$F \equiv \frac{d / d_g - H}{1 + H}, \tag{3.2}$$

replaces H as the relevant heat transfer coefficient. Nepomnyashchii & Simanovskii (1990) and Golovin, Nepomnyashchy & Pismen (1997) revisited the two-layer model and found the same linear instability onset. This two-layer prediction (3.1) agrees better with experiment (see §5) than the onset predicted by the one-layer model (2.2).
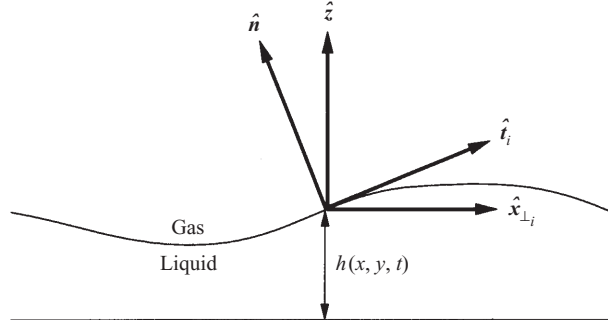
FIGURE 3. Sketch defining directions. $\hat{x}_{\perp,i} \equiv (\hat{x}, \hat{y})$ and $\hat{z}$ are Cartesian coordinates defined globally. The directions $\hat{n}$ and $\hat{t}_i$ are, respectively, the directions normal and tangent to the surface (the two tangent directions are indexed by i).

We introduce here a two-layer *nonlinear* model that gives better agreement with experiment than does the one-layer model and correctly predicts the formation of localized elevations ('high spots'), as well as localized depressions ('dry spots'). The two-layer model takes into account the full effect of the deformation upon the surface temperature profile. In the one-layer model, an elevated region of the interface is cooler because it is farther from the heater; in the two-layer model, an elevated region of the interface is even cooler (than in the one-layer model) because the elevated region is also closer to the cool upper plate. That is, the two-layer model also takes into account the decrease in the thickness of the gas layer between the interface and the top plate, thus increasing the effect of the deformation. This additional effect increases in influence with increasing d/d_g.

3.1. *Nonlinear evolution equation*

In this section we derive a nonlinear evolution equation which encompasses both the one- and two-layer models. The two-layer model equation predicts the existence of a new state, a localized elevation, which is not predicted by the one-layer model. Figure 3 shows the notation.

We take the local interface temperature to be given by (1.4) with $d \rightarrow dh(x,y,t)$ and $d_g/d \rightarrow [d_g/d - (h(x,y,t)-1)]$, or

$$T(x,y,z=h) = T_b - \frac{T_b - T_t}{1 + \frac{(d_g/d - h(x,y,t)+1)k}{h(x,y,t)k_g}} = T_b - \frac{\Delta T\ h}{1 + F - Fh}, \qquad (3.3)$$

where $h(x,y,t)$ is non-dimensionalized by d. (The one-layer model fails to include the change in the local air depth due to variations in h; thus in the limit of $d/d_g \rightarrow 0$, where such variations would be negligible, the one- and two-layer predictions coincide.) This 'reduced' model assumes pure conduction in both liquid and gas layers, requires all disturbances to have a long wavelength so that thermal diffusion in the horizontal directions can be neglected, and ignores any viscous coupling or driven thermal convection in the upper (gas) layer. We ignore these effects in order to isolate the aspect of the full two-layer theory necessary to capture the phenomena. (For $q \ll 1$, there is no difference between this reduced theory and the full linear theory.) Temperature variations not due to deformational perturbations are ignored since G is assumed small enough that the diffusive timescale is much faster than the gravitational timescale.

The relevant equations for this system are, respectively, Navier–Stokes, temperature, continuity, velocity and temperature boundary conditions at the bottom plate, kinematic boundary condition, tangential and normal stress boundary conditions at the interface, and the temperature boundary condition at the top plate:

$$\frac{1}{Pr}\left[\frac{\partial \boldsymbol{u}}{\partial t} + (\boldsymbol{u}\cdot\nabla)\boldsymbol{u}\right] = -\nabla P + \nabla^2 \boldsymbol{u} - G\hat{\boldsymbol{z}}, \tag{3.4a}$$

$$\frac{\partial T}{\partial t} + (\boldsymbol{u}\cdot\nabla)T = \nabla^2 T, \tag{3.4b}$$

$$\nabla\cdot\boldsymbol{u} = 0, \tag{3.4c}$$

$$T = \boldsymbol{u} = 0 \ \text{at} \ z = 0, \tag{3.4d}$$

$$w = \frac{\partial h}{\partial t} + \boldsymbol{u}\cdot\nabla h \ \ \text{at} \ z = h, \tag{3.4e}$$

$$\frac{\partial S}{\partial x_{t_i}} = \left(\frac{\partial u_n}{\partial x_{t_i}} + \frac{\partial u_{t_i}}{\partial x_n}\right) \ \ (i = 1, 2) \ \text{ at } z = h, \tag{3.4f}$$

$$P - S\left(\frac{1}{R_1} + \frac{1}{R_2}\right) = 2\left(\frac{\partial u_n}{\partial x_n}\right) \ \ \text{at} \ \ z = h, \tag{3.4g}$$

$$T = -\frac{1 + H}{H} \ \ \text{at} \ z = 1 + \frac{d_g}{d}. \tag{3.4h}$$

R_1 and R_2 are the local radii of curvature of the interface. We separate the velocity into horizontal ($\boldsymbol{u}_\perp$) and vertical (w) components. In addition,

$$\nabla_\perp \equiv \hat{x}\frac{\partial}{\partial x} + \hat{y}\frac{\partial}{\partial y}.$$

Since $h(x, y)$ does not depend on z, $\nabla h = \nabla_\perp h$. All lengths are scaled by d, time by d^2/κ, velocities by κ/d, pressure by $\rho\nu\kappa/d^2$, temperatures by ΔT, and surface tension by $\rho\nu\kappa/d$. In the absence of deformation, the dimensionless surface tension is $S \equiv \sigma d/\rho\nu\kappa = Cr^{-1}$, where Cr is the Crispation number. The dimensionless gravitational acceleration is G, the Galileo number. The temperature derivative of surface tension is non-dimensionalized so that $-\partial S/\partial T \equiv M$ (the liquid is assumed Boussinesq, which is a good approximation in our experiments). The height of the interface $h(x, y)$ is non-dimensionalized by the mean liquid depth d, so $h(x, y) = 1$ is the undeformed state. We assume that the change in surface tension is small, or

$$\frac{\sigma_T \Delta T}{\sigma} = MCr \ll 1. \tag{3.5}$$

We follow the method used by Davis (1983) and expand the equations of motion in terms of the magnitude of the fundamental wavevector q ($= 2\pi d/L$), which is assumed to be small ($d \ll L$). All time derivatives and spatial derivatives in the horizontal direction are taken to be of order q; derivatives in the vertical direction are of $O(1)$. Equation (3.4c) then requires that w is one order higher in q than $\boldsymbol{u}_\perp$. We adopt the following scalings: $\boldsymbol{u}_\perp \sim O(1)$, $w \sim O(q)$, and $P \sim O(q^{-1})$. In addition, S must be of $O(q^{-3})$, $\partial S/\partial T \sim O(q^{-1})$, $G \sim O(q^{-1})$, and $Pr \geqslant O(1)$. These scalings are necessary in order that the three important effects (thermocapillarity, gravity, and

surface tension) appear at lowest order. The lowest-order equations are

$$\frac{\partial^2 \boldsymbol{u}_\perp}{\partial z^2} = \nabla_\perp P, \quad \frac{\partial P}{\partial z} + G = 0, \quad \frac{\partial^2 T}{\partial z^2} = 0, \qquad (3.6a\text{-}c)$$

$$\nabla_\perp \cdot \boldsymbol{u}_\perp + \frac{\partial w}{\partial z} = 0, \qquad (3.6d)$$

$$T = \boldsymbol{u}_\perp = w = 0 \text{ at } z = 0, \qquad (3.6e)$$

$$\frac{\partial h}{\partial t} = w - \boldsymbol{u}_\perp \cdot \nabla h \text{ at } z = h, \qquad (3.6f)$$

$$\nabla h \cdot \nabla S + (\nabla h \cdot \nabla h)\frac{\partial T}{\partial z}\left(\frac{\mathrm{d}S}{\mathrm{d}T}\right) - \nabla h \cdot \frac{\partial \boldsymbol{u}_\perp}{\partial z} = 0 \text{ at } z = h, \qquad (3.6g)$$

$$\left[\nabla h \times \nabla_\perp S - \nabla h \times \frac{\partial \boldsymbol{u}_\perp}{\partial z}\right] \cdot \hat{z} = 0 \text{ at } z = h, \qquad (3.6h)$$

$$P + S\nabla^2 h = 0 \text{ at } z = h, \quad T = \frac{-h}{1 + F - Fh} \text{ at } z = h \qquad (3.6i,j)$$

In determining the interfacial temperature profile (3.6*j*), we used (3.6*c*), which implies that the temperature profile is purely conductive and that diffusion in the horizontal direction is negligible, and thus (3.3) is a valid approximation. From (3.6*b*) and (3.6*i*), we have

$$P(\boldsymbol{x}, t) = -S\nabla^2 h + G(h - z). \qquad (3.7)$$

From (3.6*a*), we have

$$\frac{\partial^2 \boldsymbol{u}_\perp}{\partial z^2} = -S\nabla\nabla^2 h + G\nabla h. \qquad (3.8)$$

Integrating over z twice and applying (3.6*e*), we have

$$\boldsymbol{u}_\perp = (-S\nabla\nabla^2 h + G\nabla h)\tfrac{1}{2}z^2 + \boldsymbol{a}(\boldsymbol{x}_\perp, t)z. \qquad (3.9)$$

Using (3.6*g*) to find $\boldsymbol{a}$, we have

$$\boldsymbol{u}_\perp = \left(-S\nabla\nabla^2 h + G\nabla h\right)\tfrac{1}{2}z^2 + z\left(Sh\nabla\nabla^2 h - Gh\nabla h + \nabla S\right). \qquad (3.10)$$

Using (3.6*d*) and (3.6*e*), we solve for the vertical velocity:

$$w = (S\nabla^2\nabla^2 h - G\nabla^2 h)\tfrac{1}{6}z^3 - \tfrac{1}{2}z^2\left[S\nabla\cdot\left(h\nabla\nabla^2 h\right) - G\nabla\cdot(h\nabla h) + \nabla^2 S\right]. \qquad (3.11)$$

Using (3.6*f*), we obtain $\partial h/\partial t$. We rescale the domain of both x and y to $[0, 2\pi)$, so that the wavevectors q become integers. In addition, time is rescaled by $G(L/2\pi d)^2/3$ to $G(L/2\pi)^2/3\kappa$. The final two-dimensional evolution equation for the local liquid depth $h(x, y, t)$ is then

$$\frac{\partial h}{\partial t} + \nabla \cdot \left\{ \frac{3D}{2} \frac{(1 + F)h^2\nabla h}{(1 + F - Fh)^2} - h^3\nabla h + \frac{h^3}{B}\nabla^2\nabla h \right\} = 0, \qquad (3.12)$$

where F is given by (3.2), D is the inverse dynamic Bond number given by (1.3), and B is the static Bond number, $B \equiv \rho g(L/2\pi)^2/\sigma > 0$. The first term in curly brackets describes the effect of thermocapillarity; the second, gravity; and the third, surface tension.

The equation of Davis (1983, 1987) is recovered for $F = 0$; the one-layer model equation (Kopbosynov & Pukhnachev 1986; Oron & Rosenau 1992; Deissler & Oron
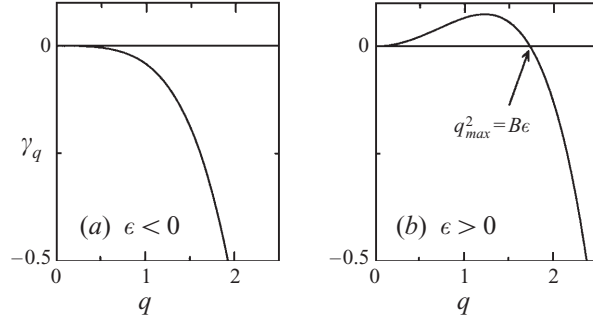
FIGURE 4. Growth rates γ_q as a function of q for (a) ϵ negative ($\epsilon = -0.01$) and (b) ϵ positive ($\epsilon = 0.1$) according to linear, long-wavelength theory ($B = 30$).

1992) is recovered for $d/d_g \to 0$, i.e. $F = -H/(1 + H)$; thus the one-layer equation always has $F \leqslant 0$, while F can be (and usually is) positive in the two-layer model. In both one- and two-layer models, $F > -1$. For $F > 0$, there is a restriction that $h(x, y) < (1 + d_g/d) < (1 + F)/F$. Also, the fluid cannot penetrate the bottom plate, or $h(x, y) > 0$. (This is enforced in the equation by $\partial h/\partial t = 0$ if $h = 0$.)

Equation (3.12) is fourth order and thus needs four boundary conditions. Two can be obtained by assuming that the sidewalls pin the meniscus of the liquid, or

$$h(0) = h(2\pi) = 1.$$

However, there is no clear choice for the second pair of boundary conditions. For the rest of this paper, we will use periodic boundary conditions, which greatly simplify the analysis.

3.2. Linear analysis

The linearization of (3.12) is

$$\frac{\partial h}{\partial t} + \epsilon \nabla^2 h + \frac{1}{B} \nabla^2 \nabla^2 h = 0, \tag{3.13}$$

where

$$\epsilon \equiv \frac{M(1 + F) - 2G/3}{2G/3} = \frac{3D(1 + F)}{2} - 1. \tag{3.14}$$

Assuming a linear solution $h = 1 + \eta_{q_1, q_2} e^{\gamma_q t} e^{i(q_1 x + q_2 y)}$, one obtains the growth rate of the qth mode ($q^2 = q_1^2 + q_2^2$),

$$\gamma_q = q^2 \left(\epsilon - q^2/B \right) \equiv q^2 \epsilon_q, \tag{3.15}$$

where ϵ_q is the control parameter appropriate for a mode of finite wavenumber q. Since modes with $q > 0$ begin to become unstable for $\epsilon > 0$ (see figure 4), the linear stability analysis of (3.12) agrees with the two-layer linear stability analysis of the full equations (3.1) for $q = 0$.

The linear stability analyses of Takashima (1981b) and Pérez-García & Carneiro (1991) predict the existence of an oscillatory instability for $M < 0$. For $PrCr \ll 10^{-3}$, Takashima (1981b) predicts that this oscillatory instability will appear with a long wavelength. Since only even derivatives of q appear in (3.13), (3.12) does not contain any oscillatory instabilities (complex γ_q). The frequency of an oscillatory mode would have to be small ($\sim q$) for the assumption of slow time scale made in the derivation to be correct. However, the long-wavelength oscillatory instability
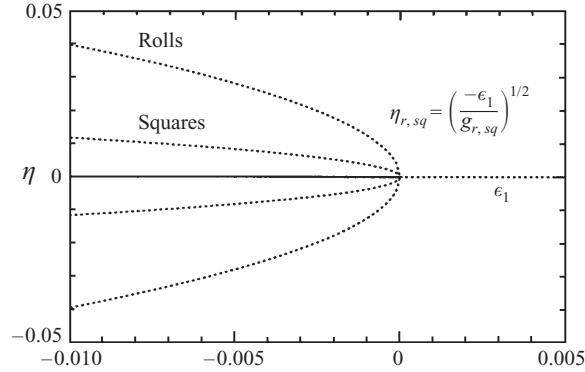
FIGURE 5. Predicted subcritical bifurcation of the long-wavelength mode according to weakly nonlinear analysis ($F = 0$, $B = 30$) for both rolls and squares. Solid lines correspond to linearly stable states; dotted lines to linearly unstable states.

predicted by Takashima (1981*b*) and Pérez-García & Carneiro (1991) has a fast (not $O(q)$) frequency and so cannot be described by (3.12).

3.3. *Weakly nonlinear analysis*

To determine the nature of the bifurcation, we performed a weakly nonlinear analysis of the evolution equation by considering just the two lowest-order wavenumbers in the deformation:

$$h = 1 + (\eta_{10}e^{ix} + \eta_{01}e^{iy} + \eta_{11}e^{i(x+y)} + \eta_{1-1}e^{i(x-y)} + \eta_{20}e^{2ix} + \eta_{02}e^{2iy}) + \text{c.c.} \qquad (3.16)$$

We are interested in when the lowest-order finite mode ($q = 1$) becomes unstable, so we use

$$\epsilon_1 = \epsilon - 1/B \qquad (3.17)$$

as our bifurcation parameter. We assume that $(\eta_{10}, \eta_{01}) \sim O(|\epsilon_1|^{1/2})$ and $(\eta_{11}, \eta_{1-1}, \eta_{20}, \eta_{02}) \sim O(|\epsilon_1|)$. Inserting the above expression for $h(x, y)$ into the evolution equation, keeping only the lowest-order terms and matching arguments of the exponentials, we find that

$$\epsilon_1\eta_{10} = -\eta_{10}\left[g_r|\eta_{10}|^2 + (g_{sq} - g_r)|\eta_{01}|^2\right], \qquad (3.18a)$$

$$\epsilon_1\eta_{01} = -\eta_{01}\left[g_r|\eta_{01}|^2 + (g_{sq} - g_r)|\eta_{10}|^2\right], \qquad (3.18b)$$

where

$$g_r = \frac{B+1}{6B}[(B+7) - 4F(B+4) + 2F^2(2B+11)], \qquad (3.19a)$$

$$g_{sq} = \frac{B+1}{6B}[(13B+31) - 4F(13B+22) + 2F^2(26B+53)]. \qquad (3.19b)$$

The two solutions of this equation are rolls ($\eta \equiv \eta_{10}$, $\eta_{01} = 0$, or vice versa) and squares ($\eta \equiv |\eta_{10}| = |\eta_{01}|$). For all values of F and B (> 0), $g_{sq} > g_r > 0$; thus the bifurcation is predicted to be a subcritical pitchfork for both rolls and squares (see figure 5), with the squares branch always closer to the axis than the rolls branch. Since g_r and g_{sq} have their minimum at $F = 1/2$ for $B > 10$, the unstable branches are farthest from the ϵ_1 axis for $F = 1/2$. In addition, for large B, both of the g are approximately linear with B and so the unstable branches are closer to the axis for large B than for small B.

In addition, the secondary (and higher-order) modes are slaved to the primary mode by

$$\eta_{11} = 2\left(F - \tfrac{1}{2}\right)(1 + B)\eta_{10}\eta_{01}, \tag{3.20a}$$

$$\eta_{20} = \left(F - \tfrac{1}{2}\right)\tfrac{1}{3}(1 + B)\eta_{10}^2, \tag{3.20b}$$

with analogous equations for η_{1-1}, η_{02}, etc.... Since all the higher-order modes change sign at $F = 1/2$, one expects that the structure of the pattern will change there. Since $F \leqslant 0$ for the one-layer model, experimental observation of such a change in the pattern would be strong evidence for the two-layer nonlinear model.

3.4. *One-dimensional potential theory (rolls)*

The weakly nonlinear theory is valid only for small ϵ_1. To look for steady states beyond small ϵ_1, we integrate (3.12) three times to formulate the problem in terms of a potential (Oron & Rosenau 1992; Deissler & Oron 1992). Once again, we assume periodic boundary conditions. We write the evolution equation as

$$\frac{\partial h}{\partial t} + \nabla \cdot \left\{ f(h)\nabla h + \frac{g(h)}{B}\nabla^2\nabla h \right\} = 0, \tag{3.21}$$

where $f(h)$ and $g(h)$ are determined from (3.12). We are interested in steady states so $\partial h/\partial t = 0$, and

$$\left\{ f(h)\nabla h + \frac{g(h)}{B}\nabla^2\nabla h \right\} = C(x, y), \tag{3.22}$$

where $\nabla \cdot C(x, y) = \nabla \times C(x, y) = 0$ ($\nabla \times C = 0$ since $\nabla \times \nabla h = 0$). In one dimension (rolls), C must be a constant, which one can show must be zero since $g(h) > 0$ and

$$\int \left(\frac{f}{g}\right)\left(\frac{\partial h}{\partial x}\right)\mathrm{d}x + \int \left(\frac{1}{B}\right)\left(\frac{\partial^3 h}{\partial x^3}\right)\mathrm{d}x = \int \left(\frac{C}{g}\right)\mathrm{d}x = 0.$$

In two dimensions, C can be zero, but it is not required to be zero, so for the remainder of this section we will consider only one-dimensional solutions where $\eta_q \equiv \eta_{q0}$ and $\eta_{0q} = 0$, or vice versa. If we define a potential V such that

$$\frac{\mathrm{d}^2 V}{\mathrm{d}h^2} \equiv \frac{f(h)}{g(h)}, \tag{3.23}$$

then

$$V = \frac{1 + \epsilon}{(1 + F)^2} h \log\left\{ \frac{h}{[1 - Fh/(1 + F)]} \right\} - \frac{h^2}{2} - Kh, \tag{3.24}$$

where K is an arbitrary integration constant, and

$$\left(\frac{\mathrm{d}^2 V}{\mathrm{d}h^2}\right)\frac{\mathrm{d}h}{\mathrm{d}x} + \frac{1}{B}\frac{\mathrm{d}^3 h}{\mathrm{d}x^3} = 0. \tag{3.25}$$

Integrating (3.25), one gets

$$\frac{\mathrm{d}^2 h}{\mathrm{d}x^2} = -B\left(\frac{\mathrm{d}V}{\mathrm{d}h}\right). \tag{3.26}$$

Upon multiplying both sides of (3.26) by $\mathrm{d}h/\mathrm{d}x$ and integrating, the final result is

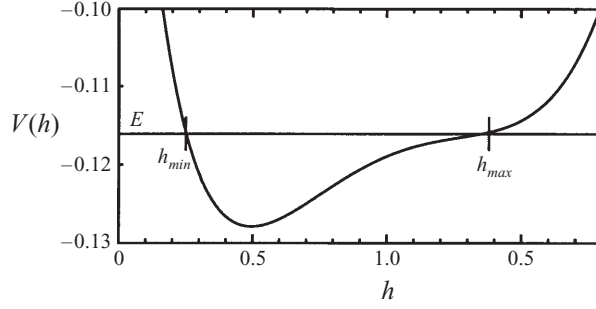$$E = \frac{1}{2B}\left(\frac{\mathrm{d}h}{\mathrm{d}x}\right)^2 + V(h, K, F, \epsilon), \tag{3.27}$$

FIGURE 6. A typical $V(h)$ curve ($K = -0.21$, $E = -0.0116$, $F = 0.5$, $\epsilon = -0.05$). The minimum and maximum heights, h_{min} and h_{max}, respectively, can be determined from $V(h) = E$.

where E is the integration constant from the last integral. The two integration constants K and E either determine or can be determined from the smallest (h_{min}) and largest (h_{max}) values of h (see figure 6):

$$K = \frac{V(h_{max}, K = 0) - V(h_{min}, K = 0)}{h_{max} - h_{min}}, \qquad (3.28a)$$

$$E = V(h_{min}, K) = V(h_{max}, K). \qquad (3.28b)$$

Equation (3.27) can be inverted to find $h(x)$. The problem is now that of a particle moving in a potential well, with two integral quantization conditions on its possible orbits. First, any solution $h(x)$ must obey the continuity equation, or

$$\int_0^{2\pi} (h-1)\mathrm{d}x = 2q \int_{h_{min}}^{h_{max}} (h-1)\left(\frac{\mathrm{d}x}{\mathrm{d}h}\right)\mathrm{d}h \propto \int_{h_{min}}^{h_{max}} \frac{(h-1)\mathrm{d}h}{(E-V)^{1/2}} = 0. \qquad (3.29)$$

Secondly, the solution must fit into the box, or

$$2q \int_{h_{min}}^{h_{max}} \left(\frac{\mathrm{d}x}{\mathrm{d}h}\right)\mathrm{d}h = \int_{h_{min}}^{h_{max}} \frac{2q\,\mathrm{d}h}{(2B(E-V))^{1/2}} = 2\pi, \qquad (3.30)$$

where the fundamental wavenumber q is an integer. Any pair of values (h_{min}, h_{max}) that satisfy the two integral conditions should be a steady state of the evolution equation. Solutions with $q > 1$ correspond to higher-order modes, and are equivalent to the fundamental mode ($q' = 1$) of a system with $B' = B/q^2$. Whenever the first condition (3.29) is satisfied, the second condition (3.30) is automatically satisfied for some B. Thus we can look for anywhere in (h_{min}, h_{max}) space where (3.29) is satisfied and then calculate

$$\frac{q}{B^{1/2}} = \pi \left\{ \int_{h_{min}}^{h_{max}} \frac{\mathrm{d}h}{(2(E-V))^{1/2}} \right\}^{-1}. \qquad (3.31)$$

The solutions $h(x, y; \epsilon, B, F, h_{min}, h_{max})$ can be constructed from (3.27) and must then be checked to see whether they are stable or unstable (see §3.4). It is clear from (3.24) that no solution can exist at $\epsilon = -1$ ($M = D = 0$) since there would be no potential well.

We checked a number of characteristic values of F for $B = 30$. Our experimental value of B is 18. We begin with the solution from weakly nonlinear analysis and quasi-statically step backwards in ϵ to continue the bifurcation curve to finite ϵ_1 (see figure 7). We also searched in (h_{min}, h_{max}) parameter space for a number of values of ϵ to find solution branches not connected to the main bifurcation branch; we then
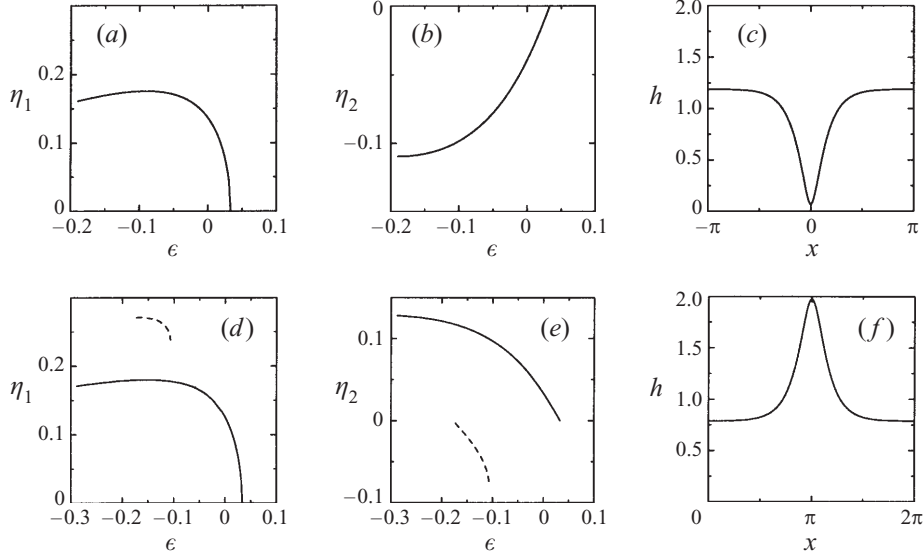
FIGURE 7. Predicted unstable stationary branches [η_1 vs. ϵ (a, d) and η_2 vs. ϵ (b, e)] of the long-wavelength mode and the (unstable) steady-state solution at $\epsilon = -0.19$ (c, f), according to potential theory. $(a$–$c)$ $F = 1/3$, $(d$–$f)$ $F = 2/3$. The bifurcation curves agree with weakly nonlinear theory for $|\epsilon_1| = |\epsilon - 1/B| \ll 1$. The curve for $F = 1/3$ terminates at $\epsilon = -0.2$ because the solution has become unphysical $(h \leqslant 0)$. The curve for $F = 2/3$ terminates at $\epsilon = -0.29$ because solutions in the potential well can no longer satisfy the conservation of liquid condition. The dashed lines in (d, e) belong to a solution that is unrelated to the main bifurcation curve (——) that starts at $\epsilon_1 = 0$. This unconnected solution, which exhibits significant depression and elevation, is similar to a combined localized depression and elevation which is seen in the simulations only for F very close to the transition from localized depression to localized elevation.

quasi-statically stepped in ϵ from any new solutions found this way. For $F < 0.525$, the main bifurcation curve corresponds to a localized depression (see figure 7 a–c). The bifurcation curve continues backwards in ϵ until $h_{min} = 0$, at which point the solution is no longer physical. Solutions for smaller (more negative) ϵ would be non-physical because the solutions $h(x)$ would be non-analytic (have a cusp at $h = 0$). One can analytically show that no localized depression solutions satisfying (3.29) exist for $\epsilon < (F - 1)/2$. For $F > 0.525$, the bifurcation curve corresponds to a localized elevation and continues backwards in ϵ until a potential well satisfying (3.29) and (3.30) no longer exists (see figure 7 d–f).

The backwards, unstable branch does not turn over into a stable branch (via a saddle-node bifurcation) for any value of F. We found no stable deformed states, which agrees with the result of Oron & Rosenau (1992) that no stable deformed state exists for $F = 0$.

3.5. *Numerical simulations*

We numerically simulated (3.12) with both one- and two-dimensional interfaces. We used a spectral method in order to enforce the (integral) continuity condition (3.29); Fourier series were the natural basis function since we used periodic boundary conditions, and Fourier series automatically satisfy (3.29) if the amplitude of the $q = 0$ mode is set to zero (η_0 or $\eta_{00} = 0$). The simulation employed a pseudospectral method to handle the nonlinear terms. Because of the fourth-order nonlinearity, a 2/5 rule (equivalent to the 2/3 rule for quadratic nonlinearities; see Canuto *et al.* 1987) was
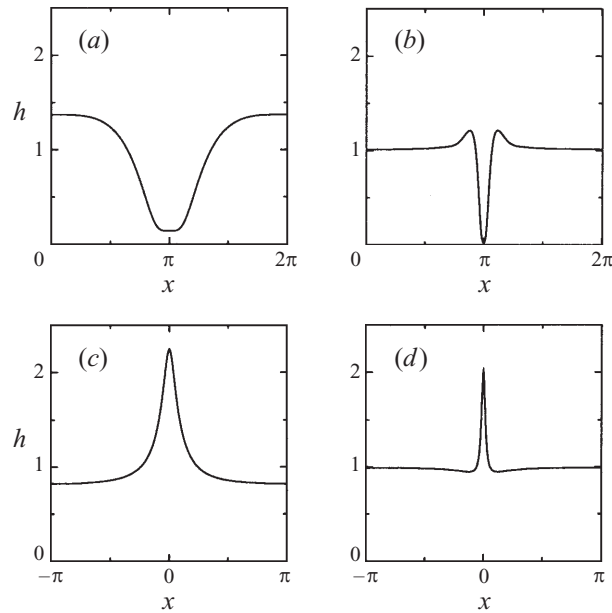
FIGURE 8. Profile of the long-wavelength mode just before rupture from one-dimensional simulations of the two-layer model at 0.33% above the onset of linear instability ($\epsilon_1 = 0.0033$). (*a*) Dry spot with $F = 1/3$ and $B = 30$, (*b*) dry spot with $F = 1/3$ and $B = 1000$, (*c*) high spot with $F = 2/3$ and $B = 30$, (*d*) high spot with $F = 2/3$ and $B = 1000$.

required to prevent aliasing (e.g. for 128 spatial locations, only 51 spectral modes q from -25 to $+25$ were used). At each time step, the power in the remaining 3/5 of modes was set to zero.

The basic results of the numerical simulations are as follows.

(1) A dry spot forms for $F <\approx 1/2$ (figures 8 *a*, *b* and 9 *a*), while for $F >\approx 1/2$ a high spot forms, which physically would pop up to the top plate (figures 8 *c*, *d* and 9 *b*). Thus, the prediction of weakly nonlinear and potential theory for the two-layer model is also observed in the simulations. (The one-layer model predicts only dry spots since $F \leqslant 0$.) The transition does not necessarily occur exactly at $F = 1/2$ (where the transition occurs depends on B, ϵ, and the initial condition), but it usually occurs close to $F = 1/2$. For example, in the potential theory (§3.4), the unstable branch of the backwards bifurcation curve did not switch from depressed region to elevated region until $F = 0.525$.

(2) The structure of the dry spot (or high spot) does not depend strongly on F far from $F = 1/2$. (Thus, in the one-layer model, there is little shape dependence on H.) Near $F = 1/2$, the system has difficulty deciding whether to form a high or dry spot, and the states look like a combination of the two (similar to the state mentioned in §3.4 for the unconnected branch in figure 7 *d*, *e*), until one finally wins out. The deformation in both directions (depression, elevation) is of similar magnitude for most of the system's evolution and thus dry spots are necessarily wider than for $F \ll 1/2$ in order to compensate for the larger positive elevation of the surrounding region.

(3) The size of a localized depression or localized elevation depends on the static Bond number B, which gives the relative strengths of gravity and surface tension. High surface tension (B small) prevents sharp structures from forming (figure 8 *a*, *c*).
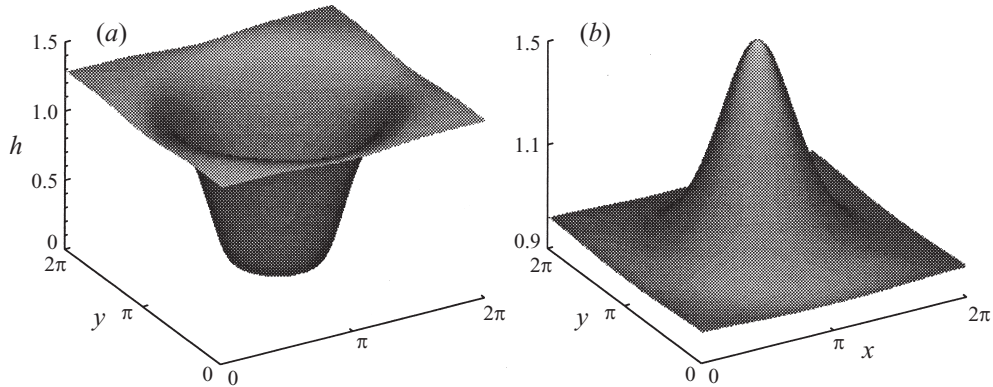
FIGURE 9. Two-dimensional profile of the long-wavelength mode just before rupture for 5% above linear instability ($\epsilon_1 = 0.05$). (a) Dry spot with $F = 1/3$ and $B = 30$, (b) high spot with $F = 2/3$ and $B = 30$.
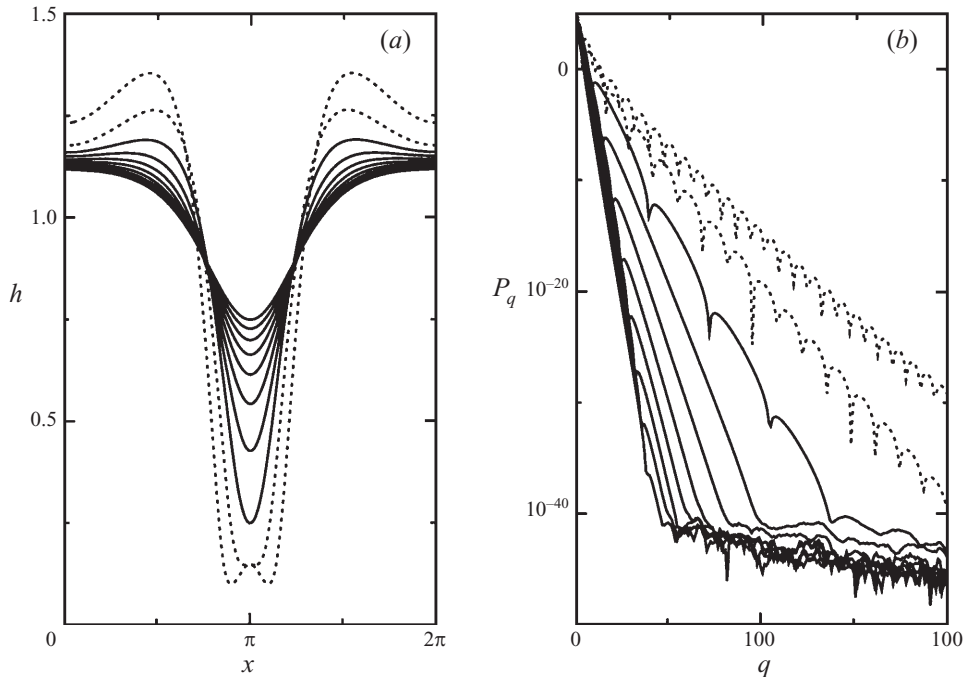

FIGURE 10. Time-evolution of a dry spot in x- and q-space ($F = 0.1$, $B = 30$, $\epsilon = 0.05$, N=1024). Lines are separated by time intervals of 1.0, beginning at $t = 136.4$ after the initial condition $h = 1 + 0.01 \cos x$. (a) Formation of a dry spot, where later times have a larger deformation. ($N = 128$ gives nearly the same curves.) (b) Power ($P_q \equiv \eta_q \eta_q^*$) in spectral modes as the dry spot forms. Spectral convergence has been lost in the last few images (dotted lines). For 75% deformation ($h_{min} = 0.25$) the spectral modes still converge; for larger deformations, there is significant power in every spectral mode.

A low surface tension (B large) allows the formation of sharp structures (figure 8 b,d).

(4) The bifurcation is subcritical for all values of F and B. For $-1/B < \epsilon_1 < 0$, the simulations agree with the weakly nonlinear analysis as to the location of the unstable
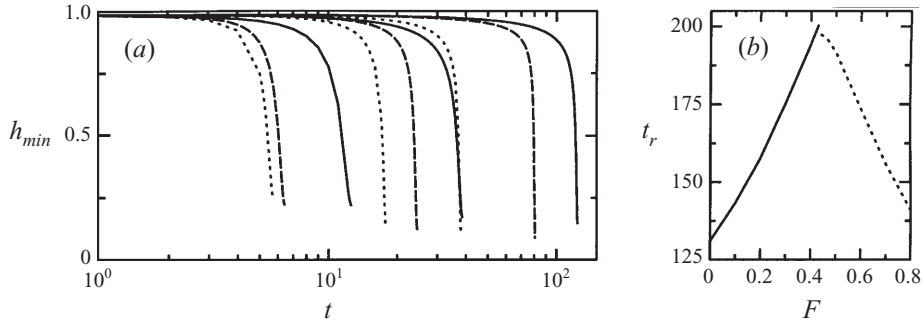
FIGURE 11. Minimum height (h_{min}) of the interface as a function of time for $F = 0.1$, $N = 128$, and (*a*) various values of B and ϵ, where ϵ for fixed B increases from right to left. ——, $B = 30$ and $\epsilon = 0.05$, 0.10, and 0.245; - - -, $B = 100$ and $\epsilon = 0.05$, 0.10, and 0.245; – –, $B = 100$ and $\epsilon = 0.0267$, 0.0767, and 0.2217 (which are the same ϵ_1 as for the $B = 30$ lines). The initial condition was $h = 1 + 0.01(\sin x + \cos x) + 0.001(\sin 2x + \cos 2x)$. (*b*) The dependence of the rupture time t_r on F ($B = 30$, $N = 128$, $\epsilon = 0.05$). (For this graph, we used $h_{min} = 0.3$ or $h_{max} = 1.5$ to define the rupture point.) Dry spots (——) form for $F < 0.44$; high spots (- - -), for $F \geqslant 0.44$. t_r decreases with increasing $|F - 0.44|$. The initial condition was $h = 1 + 0.01 \cos x$.

branch. The simulations also find the same unstable branch found by the potential theory. Location and stability of solution branches are determined in the simulation by integrating in time two initial conditions with slightly different deformation. When the initial conditions straddle the unstable solution, the solutions diverge in time with the deformation increasing in one and decreasing in the other. No stable, deformed states are ever seen in either one or two dimensions.

(5) The physics that stabilizes the dry spot in the experiments is not contained in the evolution equation. When $h_{min} \to 0$ for $F < 1/2$ (or $h_{max} \to (1+F)/F$ for $F > 1/2$), the power in the higher-order modes begins to dominate, spectral convergence is lost, and the simulation breaks down (see figure 10). Other equations of this type have been shown to exhibit such finite-time singularities (Bertozzi *et al.* 1993; Goldstein, Pesci & Shelley 1995).

(6) The simulation begins with an initial perturbation of order 1%. If unstable, the perturbation grows at a rate determined by ϵ_1; when the higher-order modes are sufficiently large, the minimum height of the interface (for $F < 1/2$) drops rapidly (see figure 11*a*). For $F > 1/2$, the maximum height of the interface increases rapidly. The larger ϵ, the faster the system forms the dry spot or high spot. The smaller ϵ, the faster the decrease (or increase for $F > 1/2$) when it occurs – when ϵ_1 is small, the harmonics (e.g. η_2, η_3) have longer to grow in amplitude than when ϵ_1 is large. Simulations with large B go unstable faster than those with small B for the same ϵ and initial conditions. This B dependence is partly due to ϵ_1 being greater for large B than for small B for the same ϵ; more importantly, the larger B, the weaker the stabilizing effect of surface tension and thus the quicker the instability can form (see figure 11*a*). The time at which the interface ruptures (t_r) also depends on F (see figure 11*b*), where the interface ruptures more slowly as F approaches the dry spot–high spot transition.

(7) Since we derived the flow field ($\boldsymbol{u}_\perp$, w) in (3.10), (3.11) in order to derive (3.12), given $h(x, y; B, F, \epsilon)$, we can find $\boldsymbol{u}$. The flow-field in both a localized depression and a localized elevation region is shown in figure 12. Note how the velocity field is concentrated at the rim of the dry spot and in the centre of the high spot.
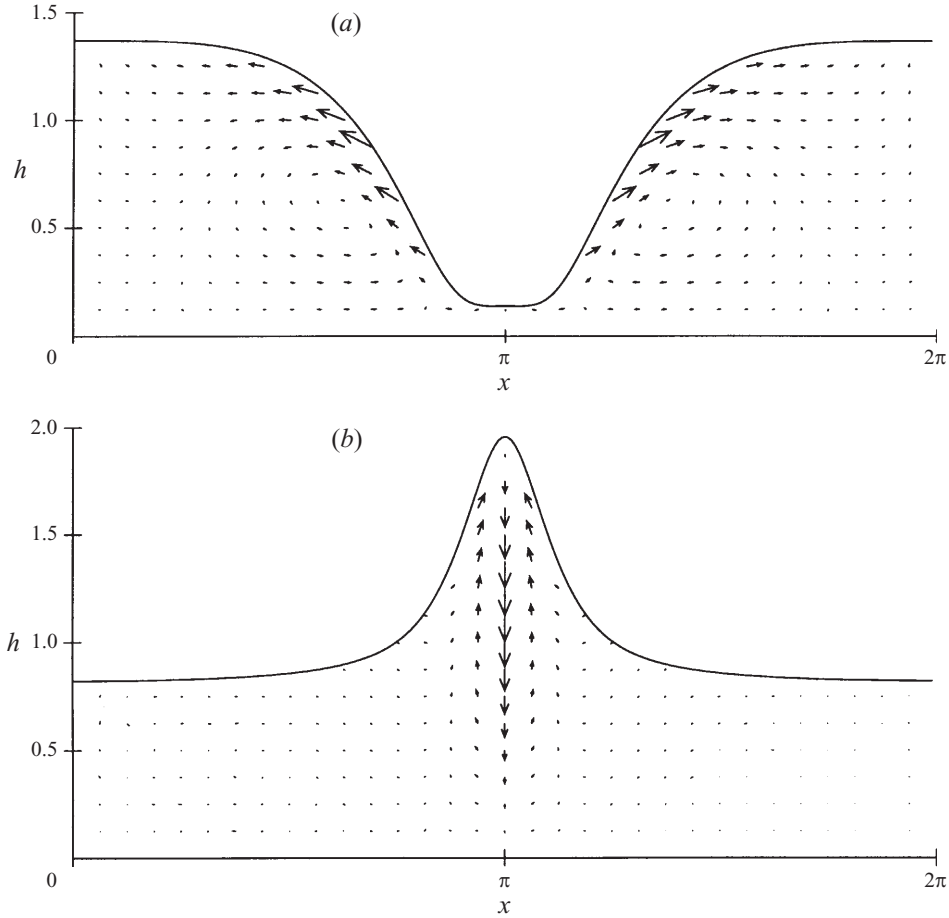
FIGURE 12. The flow field in both localized depressed and elevated regions. (*a*) A dry spot just before rupture ($F = 1/3$, $B = 30$, $\epsilon_1 = 0.0033$). The maximum velocity magnitude is 0.28, where the velocity scale is $3\kappa d(2\pi/L)^2/G$. (*b*) An elevated region just before 'pop up' ($F = 2/3$, $B = 30$, $\epsilon_1 = 0.0033$). The maximum velocity magnitude is 16.0. The *h*-axis has been stretched by a factor $\pi/2$ with respect to the *x*-axis. Since we rescaled the length of the *x*-axis from L to 2π, the velocity in the horizontal direction is really a factor of $2\pi/L$ smaller than shown.

3.6. *Effect of non-uniformity*

Previous studies (Tan, Bankoff & Davis 1990; Burelbach, Bankoff & Davis 1990) found that imposed non-uniform heating leads to stable deformations of the interface. We wish to understand the effect of a small non-uniformity in heating or cooling upon the onset of the long-wavelength instability. To model this non-uniformity, we introduce a function $\psi(x, y)$, which modulates the 'ideal' temperature drop across the liquid layer,

$$\Delta T(x, y) = (1 + \psi(x, y))\Delta T, \tag{3.32}$$

where ΔT is given by (1.4) and the non-uniformity represented by $\psi(x, y)$ can originate from either the top or bottom plate temperatures.
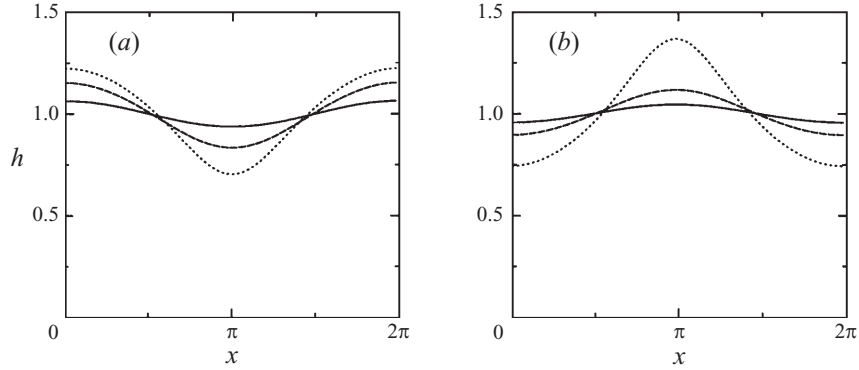
FIGURE 13. Stable, deformed steady-state solutions for $B = 30$ and $\psi_1 = 0.025$. (*a*) $F = 0.1$ and ϵ of -0.40 (——), -0.20 (— —), and -0.14 (- - -). The steady-state solution becomes unstable and evolves to a localized depression (dry spot) at $\epsilon = -0.13$. (*b*) $F = 0.6$ and ϵ of -0.40 (——), -0.20 (— —), and -0.095 (- - -). The steady-state solution becomes unstable and evolves to a localized elevation (high spot) at $\epsilon = -0.093$.

The evolution equation then becomes

$$\frac{\partial h}{\partial t} + \nabla \cdot \left\{ \frac{(1+\epsilon)(1+\psi)h^2 \nabla h}{(1+F-Fh)^2} + \frac{(1+\epsilon)h^3 \nabla \psi}{(1+F)(1+F-Fh)} - h^3 \nabla h + \frac{h^3}{B} \nabla^2 \nabla h \right\} = 0. \quad (3.33)$$

In the presence of non-uniformity ($\psi \neq 0$) and a temperature gradient across the fluid ($\epsilon > -1$), the undeformed state ($h(x, y) = 1$) is no longer a steady-state solution of the evolution equation. In general, we cannot solve analytically for the steady-state solutions, but in the limit of small deformation and non-uniformity ($|h - 1| \ll 1, |\psi| \ll 1$), we can linearize the equation:

$$\frac{\partial h}{\partial t} + \epsilon \nabla^2 h + \frac{1+\epsilon}{1+F} \nabla^2 \psi + \frac{\nabla^2 \nabla^2 h}{B} = 0. \quad (3.34)$$

In (one-dimensional) spectral space, $\psi = \sum_q \psi_q e^{iqx}$ and $h = 1 + \sum_q \eta_q e^{iqx}$. The linearized equation gives

$$\frac{\partial \eta_q}{\partial t} = q^2 \left(\epsilon_q \eta_q + \frac{1+\epsilon}{1+F} \psi_q \right), \quad (3.35)$$

which has the solution

$$\eta_q(t) = \eta_q(0) e^{q^2 \epsilon_q t} - \psi_q \frac{(1+\epsilon)q^2}{(1+F)\epsilon_q} \left(1 + e^{q^2 \epsilon_q t} \right). \quad (3.36)$$

For $\epsilon_1 < 0$, as $t \to \infty$, the steady-state solution is

$$h(x) = 1 - \frac{1+\epsilon}{1+F} \sum_q q^2 \frac{\psi_q}{\epsilon_q} e^{iqx}. \quad (3.37)$$

This equation is valid only where $|h - 1| \ll 1$, so $\epsilon_q \equiv \epsilon - q^2/B < 0$ and $|\epsilon_q| \ll 1$. The extension to two dimensions gives

$$h(x, y) = 1 - \frac{1+\epsilon}{1+F} \sum_{q_1, q_2} q^2 \frac{\psi_{q_1, q_2}}{\epsilon_q} e^{i(q_1 x + q_2 y)}, \quad (3.38)$$
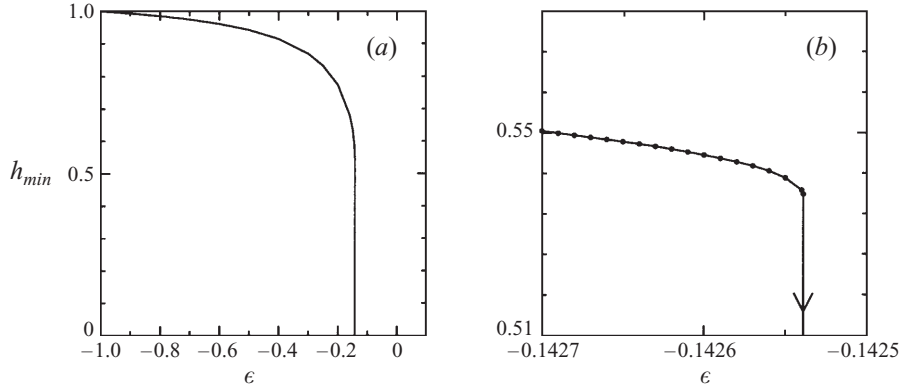
where, once again, $q^2 = q_1^2 + q_2^2$.

FIGURE 14. Minimum height h_{min} of the interface as a function of ϵ according to numerical simulations of the two-layer model with non-uniform vertical heating ($\psi_1 = 0.0375$, $F = 0.2$, and $B = 30$). The deformed state becomes unstable to a dry spot at $\epsilon = -0.142539$. (a) Full range of ϵ; (b) close-up of the region where the deformed state becomes unstable.
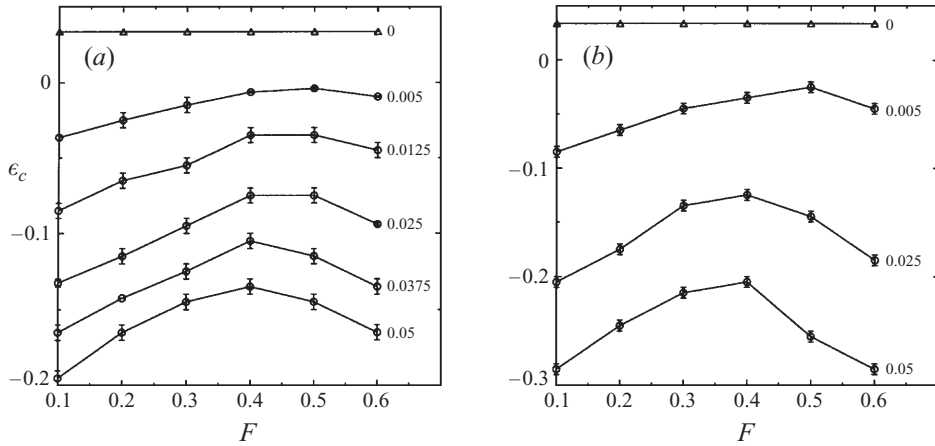

FIGURE 15. Onset ϵ as a function of F for different amounts of non-uniformity ($B = 30$). (a) various ψ_1 in one dimension, (b) various $\psi_{10} = \psi_{01}$ in two dimensions.

We can study the effect of the non-uniformity by numerically simulating the above evolution equation with the pseudospectral code discussed in the previous Section. The non-uniformity introduces a steady-state deformation with any temperature difference across the layer (see figure 13). The liquid layer still becomes unstable to the formation of a dry spot, but the bifurcation occurs from this deformed steady state, not from a perfectly flat interface (see figures 13 and 14). The non-uniformity selects where the dry spot or elevated region will form; the dry spot (or elevated region) appears at the minimum (or maximum) of the steady-state deformation. The onset of the bifurcation occurs earlier than in the absence of non-uniformity (see figures 15 and 16); to first approximation, one can consider the steady-state deformation as a finite perturbation that causes the system to intersect the unstable backwards bifurcation curve for $\epsilon_1 < 0$. For example, with $\psi = 2\psi_1 \cos x$, instability that evolves to a dry spot occurs at $\epsilon = -0.13$ (a 16% shift) for $B = 30$, $F = 0.1$, and $\psi_1 = 0.025$. In addition, the non-uniformity can shift the transition from dry spot to high spot away from $F = 1/2$ by a small amount.
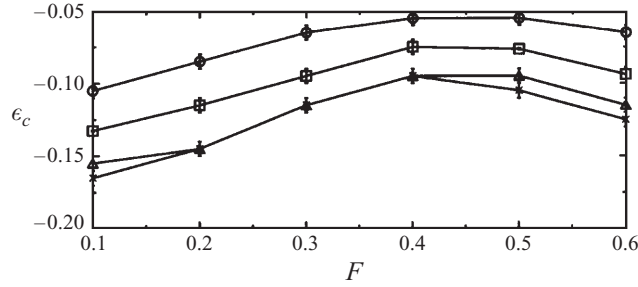
FIGURE 16. Onset ϵ as a function of F in one dimension $\psi_1 = 0.025$ and $B = 18$ (○), $B = 30$ (□), $B = 67$ (△), $B = 100$ (×).

4. Experimental system

The liquid lies on a 3.81 cm diameter, gold-plated aluminium mirror (see figure 17). The mirror is attached to an aluminium plate whose bottom is heated by a 14 Ω thin-film resistance heater. Generally, the heater power, not the temperature of the mirror, is controlled. About 30–60% of the heater power travels through the liquid (with the larger percentages occurring when helium is the gas); the remainder of the power is lost through the bottom and sides of the aluminium plate and Plexiglas cup. A thermistor in the centre of the aluminium plate measures T_b, which is stable to $\pm 0.2\,°C$.

A cooled, 3 mm thick sapphire window bounds the gas from above. The cooling system was designed to allow imaging using an infrared (3–5 µm) camera. Chloroform was employed as the cooling fluid since water and other common liquids are strongly absorbing in this wavelength range. Owing to the toxicity of this substance, a closed secondary cooling system was required (see figure 17c). Cooled chloroform is pumped between two sapphire windows (bottom, 3 mm thick; top, 1 mm thick and tilted at an angle of 1° to prevent multiple reflections and eliminate interference fringes between the two windows). The chloroform then travels through a heat exchanger that maintains the temperature of the chloroform at 21.3 $\pm$ 0.1 °C, as measured in the reservoir. The chloroform temperature was chosen to be near room temperature to minimize the demands on the secondary cooling system and to reduce changes in the chloroform temperature as it travels from the heat exchanger to the sapphire windows. (The increase in temperature of the chloroform during one complete cycle through the entire system is 0.4 °C; a 0.1 °C increase occurs between the sapphire windows and the reservoir.)

The temperature drop across the liquid ΔT is calculated from the top T_t and bottom T_b temperatures using (1.4). As mentioned in §1, ΔT equals the mean temperature drop $\langle \Delta T \rangle$ across the liquid only in the limit of small deformation. With deformation $\eta(x, y) \equiv h(x, y) - 1$, the mean temperature drop assuming conduction and neglecting horizontal thermal diffusion is

$$\langle \Delta T \rangle = \Delta T \left[1 + F(1 + F) \left\langle \eta^2 + F\eta^3 + F^2\eta^4 + ... \right\rangle \right]. \quad (4.1)$$

Thus with deformation, ΔT typically underestimates $\langle \Delta T \rangle$ for $F > 0$ and over-estimates $\langle \Delta T \rangle$ for $F < 0$. There is no difference for $F = 0$ and the over- or underestimation increases with $|F|$. For example, in figure 8, $\langle \Delta T \rangle$ is (a) 8%, (b) 1%, (c) 35%, and (d) 5% larger than ΔT. These states are near rupture, however; as the states begin to form, there is no significant difference between $\langle \Delta T \rangle$ and ΔT. In figure 10, the difference is less than 1% for all but the two most deformed states (for
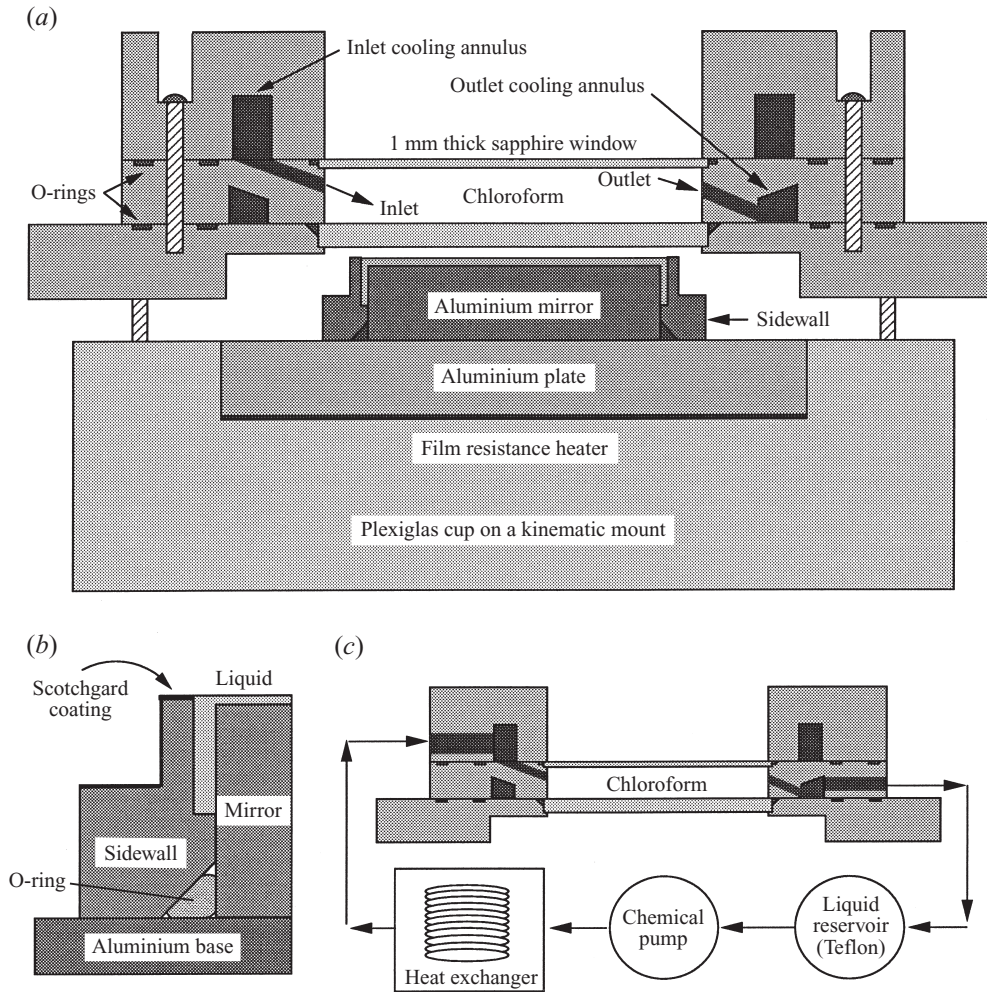
FIGURE 17. Cross-section of experimental apparatus, drawn to scale. (*a*) The complete experimental cell. Both top and bottom plates have high thermal conductivity relative to the liquid and gas. The height of the cooling system (upper part with the sapphire windows) above the liquid layer can be adjusted. The liquid depth, gas depth, and sidewall height above the mirror are shown 5 times their actual vertical size in order to make them visible on the diagram. The mirror has a diameter of 3.81 cm and a height of 0.95 cm. (*b*) Close-up of aluminium sidewall. The liquid layer shown is twice as thick as used in the experiments. We employ a narrow moat (0.1 cm wide, 0.5 cm deep) between mirror OD and sidewall ID. A thin layer of Scotchgard helps prevent the liquid from wetting the top of the sidewall. (*c*) Schematic of cooling system. A Teflon-lined pump sends chloroform through a secondary cooling loop (loops of copper pipe submerged in a temperature-controlled water bath). The chloroform is then squirted through 16 inlet jets between two sapphire windows and then removed through 16 outlet holes. Chemically resistant Viton tubing is used throughout.

which $\langle \Delta T \rangle$ is larger than ΔT by $< 2.5\%$). Ultimately, since both experiment and two-layer theory use the same definition of ΔT in defining D, there is no problem in comparing experiment and two-layer theory and $\langle \Delta T \rangle$ is essentially irrelevant.

The uncertainty in $T_b - T_t$ is approximately ± 0.3 °C, where T_t is taken to be the temperature of the chloroform as measured in the reservoir (see figure 17*c*). The uncertainty in ΔT is then $\pm 0.3 H/(1 + H)$ °C, or typically ± 0.03 °C ($< 1\%$ to 3%

of ΔT), with uncertainties approaching ± 0.06 °C (1% of ΔT) for thin air layer experiments and ± 0.15 °C (3% of ΔT) for helium gas layer experiments.

The total gap $(d + d_g)$ between the lower sapphire window and the mirror bottom is uniform to 10 fringes (3.2 μm), as verified interferometrically. The size of the gap is determined by introducing indium shims of various sizes and observing the change in the interference fringes between the window and the mirror. We consider the gap to have the same thickness as the shim when the shim does not perturb the fringes, but a slightly thicker shim (by 5 μm) does.

The liquid depth is uniform to a fringe (0.32 μm) in the central 75% of the cell at $\Delta T = 0$. The depth is measured using a stylus attached to a micrometer. The position of the upper interface is determined when the liquid suddenly wets the sharp tip of the stylus as the stylus is lowered. The stylus is then lowered further until contact with the mirror is signalled by an ohmmeter connected to the stylus and the metal mirror. The depth is measured at $\Delta T = 0$ since the temperature of the stylus must be equal to the temperature of the liquid or thermocapillary effects will cause either premature or late wetting of the stylus by the liquid. The liquid depths can be measured to ± 5 μm.

An aluminium sidewall laterally constrains the liquid. A number of different sidewall configurations are used, but most experiments are performed with a sidewall 0.015 cm taller than the mirror. Since $D \propto d^{-2}$, we increase d in a narrow annulus between the outer diameter of the mirror and the inner diameter of the sidewall (see figure 17b) to diminish the effect of the sidewall and inhibit the long-wavelength instability near the sidewall. The sidewall is most likely the largest source of non-uniformity in the system since the sidewall has a much larger thermal conductivity than does the liquid, and mechanical pinning at the sidewall introduces non-uniformities in the surface height near the edge of the cell, even at $\Delta T = 0$.

Since $G \propto v^{-1}$, to investigate the long-wavelength regime we use high-viscosity fluids. For most experiments in this paper we use a $v = 0.102$ cm^2 s^{-1} (at 50 °C) silicone oil that has been distilled once to remove low-vapour-pressure components, which can condense on the cool, upper plate (Schatz & Howden 1995). Use of a much larger-viscosity liquid increases the difficulty of the experiments by increasing the relaxation time of the liquid. The predicted viscosity independence of onset is tested in experiments with silicone oils of viscosity $v \approx 0.25$–0.30 cm^2 s^{-1} at 50 °C. Infrared images are made using an infrared-absorbing (at 4.61 μm with an extinction length of order a few microns) polymethylhydrosiloxane silicone oil with $v \approx 0.25$ cm^2 s^{-1} at 50 °C.

Liquid depths range from 0.007 to 0.027 cm. Surface tension is clearly the driving force since $M/R \geqslant 100$, where the Rayleigh number is $R \equiv \alpha g \Delta T d^3 / v \kappa$ and α is the volume coefficient of expansion of the liquid (Davis & Homsy 1980).

Gas layer thicknesses range from 0.02 to 0.10 cm. The gas in the upper layer is typically air, although a few experiments employ helium gas. The helium is slowly leaked into the apparatus, which is covered by a skirt of plastic wrap. We use helium since it has a large thermal conductivity (slightly larger than that of silicone oil), so $H \approx d/d_g$ and $F \approx 0$. Thus, $F \ll 1/2$ for even very large d/d_g where, in air, $F \gg 1/2$. This F difference between air and helium becomes useful in studying the predicted transition between dry spots and high spots at $F = 1/2$.

We use an optical system (see figure 18) that serves as both an interferometer and a shadowgraph (see, for example, Rasenat *et al.* 1989). When the deformation is small, we use the optical system as an interferometer to give an indication of the deformation of the interface. The mirror–window fringes are much
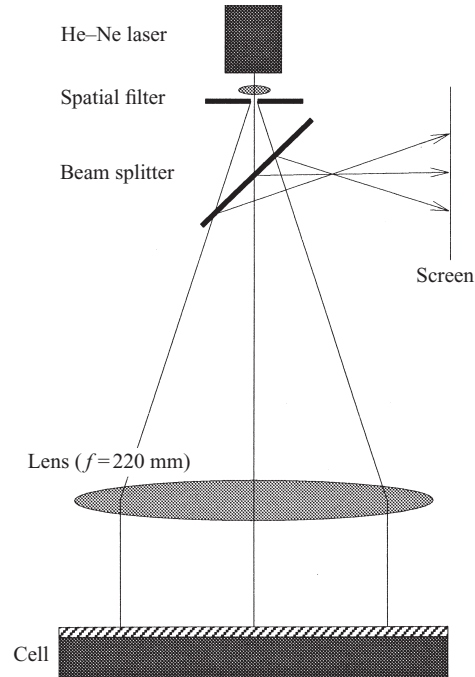
FIGURE 18. Combination shadowgraph and interferometer used in experiment (not to scale). For infrared imaging, the laser is turned off, the 220 mm lens is removed, a gold-plated mirror replaces the beam splitter, and the infrared camera replaces the screen.

stronger than the mirror–liquid fringes, so it is difficult to count the mirror–liquid fringes to get a quantitative measure of the deformation. When the deformation is large, we use the optical system as a shadowgraph, where deformation acts as a lens to focus the incident light. The initial formation of a localized depression is signalled by a bright spot on the shadowgraph image. Once the interface is significantly deformed (as the liquid is in the process of forming a dry or high spot), the deformation can be seen by eye. A fully formed dry spot can easily be seen by eye. For making images used in this paper, we employed a 256×256 pixel Amber Engineering Proview 5256 LN$_2$-cooled InSb infrared staring array sensitive in a 0.08 μm band centred around 4.61 μm. The brightness temperature measured by the camera does not give the interface temperature since the emissivity depends on the curvature of the interface. However, the brightness temperature gives an approximate measure of the interfacial temperature field.

5. Experimental results

We see four distinct states at onset of instability: the two long-wavelength modes of dry spots (figure 19a) and high spots (figure 19b), a mixed long-wavelength and hexagonal state (figure 19c), and hexagons (figure 19d). Section 5.1 compares the onset of the long-wavelength instability to linear stability theory. Section 5.2 describes the localized depressions (dry spots); §5.3 describes localized elevations (high spots); and §5.4 discusses the competition between the long-wavelength mode and hexagons.
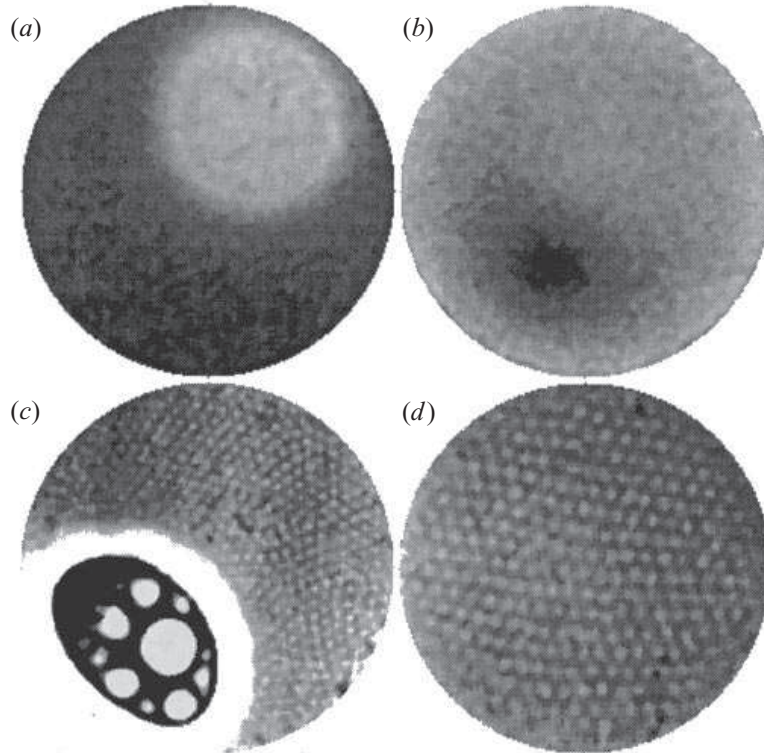
FIGURE 19. Infrared images of states seen in the experiment. The temperature increases with increasing brightness, so warm depression regions are white (except in *c*) and cool elevated regions are dark. Each image has its own brightness scale, so temperatures in different images cannot be compared. (*a*) A localized depression (dry spot) with a helium gas layer, where $d = 0.025$ cm, $G = 50$, $D(1 + F) = 0.84$, and $F = -0.06$; (*b*) a localized elevation (high spot) with an air gas layer, where $d = 0.037$ cm, $G = 160$, $D(1 + F) = 0.63$, and $F = 0.91$; (*c*) a dry spot with hexagons in the surrounding region, with an air gas layer, $d = 0.025$ cm, $F = 0.4$, $G = 101$, $D(1 + F) = 0.74$, and $M = 53$ (the dry spot looks cold since a 50/50 mixture of infrared-absorbing liquid and 0.102 cm^2 s^{-1} liquid was used and the camera sees through the liquid to the mirror, which appears cold in the infrared); (*d*) hexagons with an air gas layer, where $d = 0.045$ cm, $G = 370$, $M = 90$, $D(1 + F) = 0.43$, and $F = 0.74$.

5.1. *Comparison of onset to stability theory*

A comparison of the experimental measurements of onset to both one- and two-layer models is given in figure 20. There is clearly a discrepancy between the experiments and the one-layer theory (figure 20*a*), with the one-layer model predicting a temperature difference 65% larger than seen in the experiments. The two-layer model (figure 20*b, c*) gives good agreement with the experiments for large liquid depths ($d > \approx 0.013$ cm), but poor agreement for small liquid depths.

Since d is measured at $D = 0$, thermal expansion of the liquid will increase d as D increases. (The thermal expansion coefficient of the liquid is 40 times that of the aluminium mirror and sidewalls, so their expansion can be neglected.) Given the geometry of the moat, d increases by ≈ 0.001 cm due to a 20 °C increase (larger than the increase in most experiments) in the mean temperature of the fluid. An increase in d of 0.001 cm has little effect ($< 3\%$) on $D(1 + F)$ for the $F > 1/2$ experiments, increases $D(1 + F)$ by $\approx 5\%$ for the $F < 1/2$ experiments, and increases $D/(1 + H)$ by
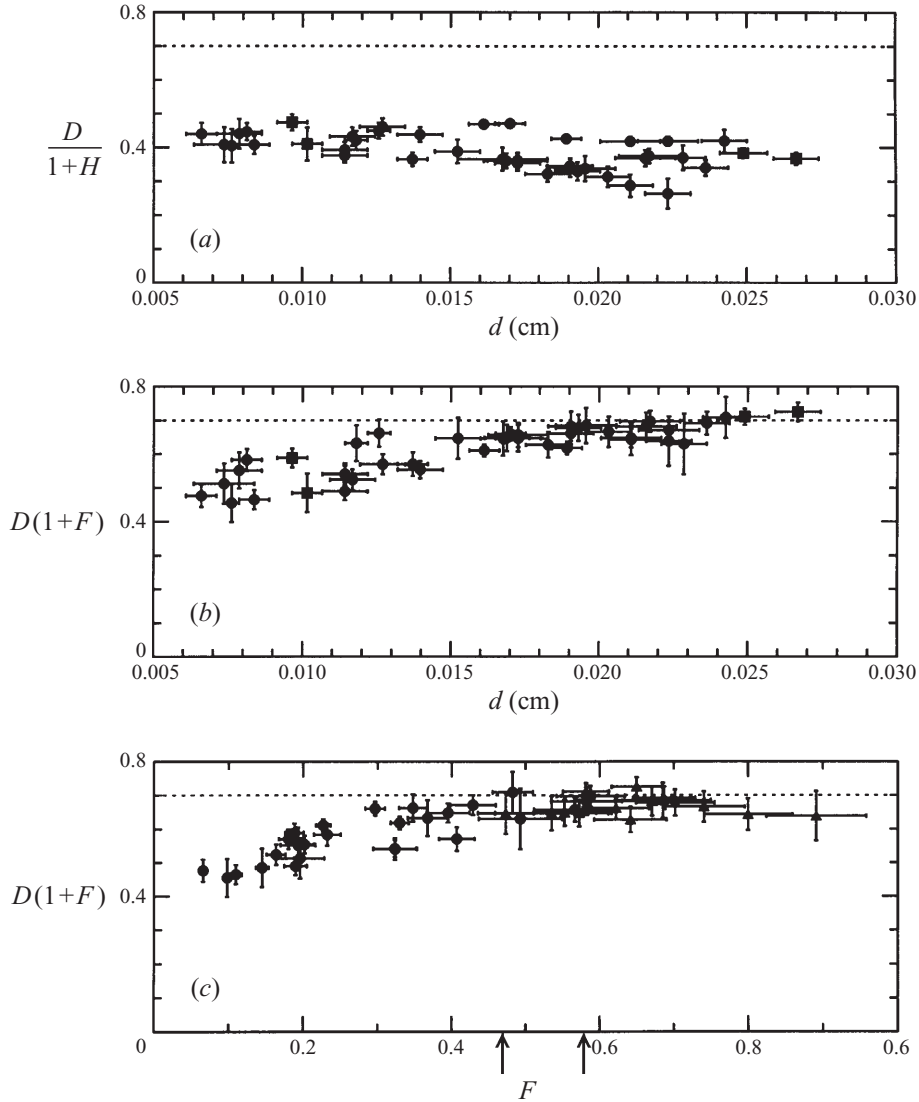
FIGURE 20. Comparison of instability onset observed with increasing ΔT (increasing D) with the predictions of (*a*) one-layer and (*b*, *c*) two-layer models. The theoretical prediction (taking into account the correction factor $(1 + 1/B)$ for finite cell size) in each case is given by the dashed line at 0.70. (*a*) The onset prediction of the one-layer model is 65% larger than observed in the experiment. (*b*) The prediction of the two-layer model gives good agreement with the experiments for thick liquid depths, but there is a significant departure for thin depths. In (*a*) and (*b*), circles are experiments in 0.102 cm^2 s^{-1} viscosity silicone oil; squares are experiments performed in higher viscosity (≈ 0.30 cm^2 s^{-1}) silicone oil. No significant difference is seen between the different viscosity fluids, in agreement with theory. (*c*) In agreement with the two-layer nonlinear theory, there is a qualitative change in the instability around $F = 1/2$, where only localized depressions (circles) form for $F < 0.48$ (left-hand arrow), only localized elevations (triangles) form for $F > 0.58$ (right-hand arrow), and both states form for $0.48 < F < 0.58$.
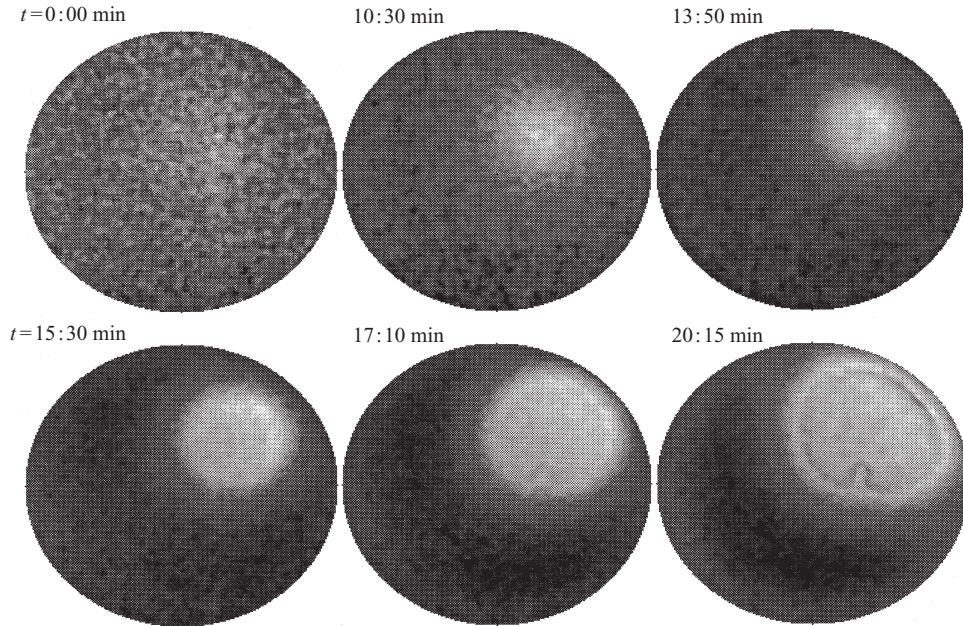
FIGURE 21. The evolution of a localized depression and formation of a dry spot in infrared-absorbing silicone oil of depth $d = 0.0267 \pm 0.0008$ cm, $F = -0.07$, $D(1 + F) = 0.81 \pm 0.04$, $D/(1 + H) = 0.41 \pm 0.03$, and helium in the gas layer. At $t = 0$ (an arbitrary starting point), there is negligible deformation of the interface. The liquid layer begins to form a localized depression (the white circle) and in 15 minutes the interface has ruptured ($h_{min} \to 0$) and formed a dry spot. The dry spot continues to grow for several more minutes before saturating. Bright regions are hot because they are closer to the heater; dark regions are cool because they are farther from the heater; all images have the same intensity scaling.

$\approx 6\% \pm 3\%$ in the one-layer theory. In addition, the values of F would be increased by less than 0.03 for $F < 1/2$ and by 0.03–0.07 for $F > 1/2$.

We do not include the onset values from the helium experiments in our data since the helium experiments are not sufficiently controlled to permit quantitative comparison with theory. Too fast a helium flow rate cools the interface and leads to artificially low values of D for onset; too slow a helium flow rate allows contamination by air and leads to artificially high values of D for onset. For example, a 40% mole fraction of air (60% helium) would lower the onset value of D in figures 19 and 21 to the value predicted by the two-layer model. (It would also increase F from -0.06 to 0.27, which is still less than 1/2.)

The steady-state deformation that we observe before the formation of the dry spot indicates the presence of a small amount of non-uniformity in the system. Even with $\psi_1 = 0.005$ (see §3.6), the interface deforms significantly ($h_{min} \approx 0.6$–0.8, depending on F) below the instability onset. Some of the variation in the onset values in the two-layer model may be due to the differing influence of non-uniformity on ϵ_c for different F (see figures 15 and 20c), but the variation in ϵ_c due to differing F is much smaller in figure 15 than in figure 20c, which implies that a constant amount of non-uniformity cannot explain the varying discrepancy between experiment and theory. We believe the sidewalls to be the largest source of non-uniformity in the system, but (3.33) cannot capture the influence of the sidewalls since we use periodic
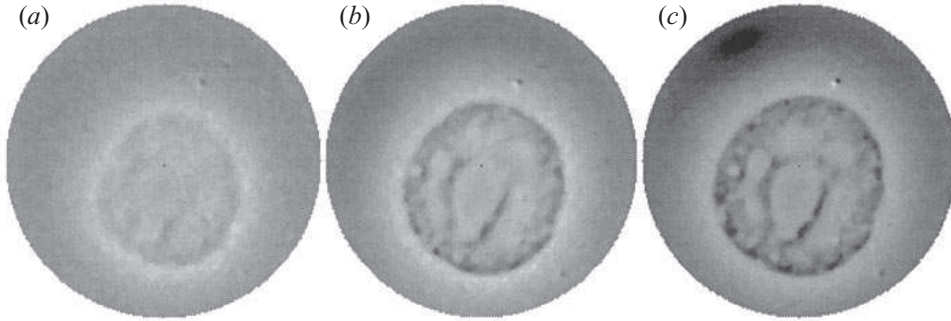
FIGURE 22. A sequence of infrared images showing the evolution of a dry spot well above onset, including the formation of a high spot. (*a*) Higher-order structures can form when ΔT is increased above $\epsilon_2 > 0$ before the dry spot has a chance to develop. (*b*) As ΔT is increased further, the dry spot slowly increases in size. (*c*) When F and D in the region surrounding the dry spot become sufficiently large, the liquid can become unstable to a high spot (upper-left corner) that pops up to the sapphire window.

boundary conditions (i.e. no sidewalls). However, §3.6 and (3.33) at least give us a sense of the effect of non-uniformity in the system.

5.2. *Localized depressions (dry spots)*

In most experiments, $F < 1/2$ and the liquid becomes unstable to a long-wavelength instability that leads to the formation of a dry spot of horizontal extent $\sim 100 \times d$ (see figures 19*a*, 20*c* and 21). The area of the dry spot is typically $1/4$–$1/3$ the area of the entire cell. Once the dry spot forms, fluid flow consists of steady-state convection concentrated at the edge of the dry spot. The dry spot is not completely dry since a very thin adsorbed layer remains (Burelbach *et al.* 1990).

The dry spot appears at different locations in different experiments, although it usually appears at the same location for multiple runs in a given experiment. When it appears near the centre of the cell, the dry spot closely approximates a circle; when it appears near the edge of the cell, it is oval-shaped with the short axis perpendicular to the sidewall. Before the formation of the dry spot, the interface exhibits steady-state deformation in a manner very similar to the non-uniformity-driven deformation shown in figure 14. Although the interface is initially flat in the central region, the sidewall causes non-uniformity at the edge of the cell even at $\Delta T = 0$; this non-uniformity grows as D (i.e. ΔT) is increased until the steady-state deformation becomes unstable, which leads to the formation of the dry spot.

Higher-order structure (such as a large droplet trapped in the centre of the dry spot) can occur when D is increased above the critical value so that higher-order modes are unstable while the dry spot forms (see figure 22*a*). Once the dry spot has formed fully, we observe no time-dependence with fixed control parameter, except an occasional slow, transient migration of the dry spot after which the dry spot remains stationary. As D is increased further, the dry spot slowly grows in size (see figure 22*b*).

5.3. *Localized elevations (high spots)*

The liquid layers in the experiment do not form dry spots for $F >\approx 1/2$ (see figure 20*c*); rather, the liquid pops up to the top plate (sapphire window). This popping up is predicted by the two-layer model, but not by the one-layer model, and the pop-up occurs consistently at the value of D predicted. In addition, the transition from dry spot to high spot occurs near the predicted value of $F = 1/2$. As seen in

the simulations (see figures 8 and 9), the size of the high spot appears to be smaller than that of the dry spot.

The liquid popping up to the top plate could be explained within the one-layer model in that when a dry spot forms, the interface surrounding the forming dry spot must increase in elevation; for example, the rim of the forming dry spot, not a localized elevation in the sense of the two-layer model, could be popping up to the top plate. This argument is plausible since $F > 1/2$ experiments have thin air layers ($d_g \approx 0.025$ cm). We addressed this question by running pairs of experiments with the same d and d_g, but with different values of F. An experiment with $F > 1/2$ in air has $F \approx 0$ in helium gas. Thus, if a dry spot forms with helium, but the liquid pops up to the sapphire window with air, that could be an indication that we are observing the predicted qualitative change of behaviour at $F = 1/2$. We obtained dry spots in helium for experiments which in air would correspond to $F = 0.75$. This suggests that the elevated regions are not the rims of dry spots popping up due to the narrow gas layer. However, it is also possible that helium's larger thermal conductivity (and thus smaller total temperature difference across the gas layer) reduces the amount of non-uniformity in the system. Alternatively, the larger heat fluxes required by helium's larger thermal conductivity may yield larger relative non-uniformities than are present with air as the gas.

Infrared imaging, however, allows us to watch a localized elevation as it accelerates upwards to the sapphire window (see figure 23) and to determine that we are observing pop-up due to a localized elevation, not the elevated rim of a forming dry spot. When the high spot begins to form, there is no evidence of a localized depression. The height of a small region of the interface begins to increase and then rapidly accelerates upwards until the liquid pops up to the top plate. In experiments with a very thin helium layer, the high spot cannot form ($F \approx 0$ in helium), but the rim of the dry spot pops up to the top plate because of the narrow gas layer. This situation is easily distinguished from the localized elevation since the entire rim (not just a small region) approaches the sapphire window; as a localized elevation forms, the rest of the interface remains far from the sapphire window.

A localized elevation can appear in the system after the formation of the dry spot when F is near but less than $1/2$. The initial dry spot drains approximately $1/3$ of the cell and thus increases the mean thickness of the remainder of the cell by 50%. This increase in h can increase the local value of F above $1/2$ and, if ΔT is increased enough (above the onset of the dry spot), then the surrounding region can become unstable to a localized elevation (see figure 22c). Although the dry spot perturbs its surrounding region, mostly by increasing the local liquid depth, its velocity field does not extend significantly past its perimeter (see figure 12a).

5.4. *Competition with hexagons*

We observe three different states at the onset of instability for $F < 1/2$. For large G (independent of F), Bénard hexagons form (figure 19d). For small G, the long-wavelength dry spot forms (figures 19a, 24). For intermediate G, both the long-wavelength (dry spot) and hexagonal modes appear together (figure 19c, 24). In this case, the long-wavelength deformational mode is linearly unstable and its formation induces the formation of the hexagonal mode by increasing the local depth in the region surrounding the dry spot. When ΔT is increased above onset for the long-wavelength mode, the dry spot continues to increase in size until either the liquid pops up to the top plate (figure 22c) or the local value of M in the surrounding elevated region is sufficiently large to cause the formation of hexagons
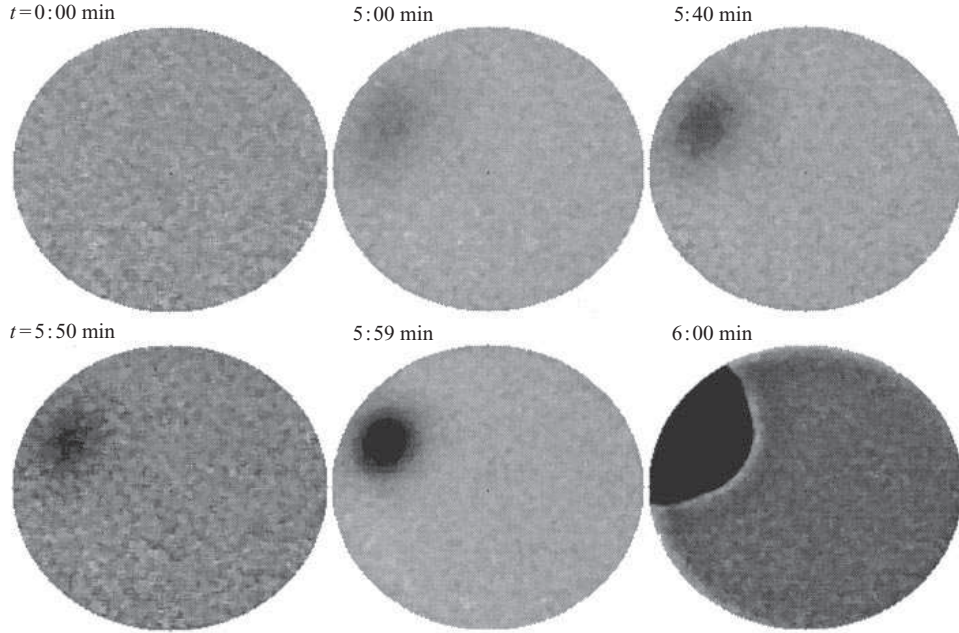
FIGURE 23. The evolution of a localized elevation and formation of a high spot that pops up to the top plate. The experiment is performed in exactly the same conditions as figure 21 except that here air was used as the gas ($F = 0.65 \pm 0.04$, $D(1 + F) = 0.73 \pm 0.03$). At $t = 0$ (an arbitrary starting point), there is negligible deformation of the interface. Five minutes later, a localized elevation (the dark oval) has begun to form, which in the span of a minute rapidly rises in elevation. At 5:59, the high spot is nearly touching the sapphire window and 1 s later the high spot has reached the sapphire window. Within 15 s (not shown), the liquid has wet nearly the entire top plate. Bright regions are hot because they are closer to the heater; dark regions are cool because they are farther from the heater; all images have the same intensity scaling.

(figure 19c); the hexagons then inhibit any further growth of the dry spot (Golovin, Nepomnyashchy, & Pismen 1994, 1997). When the hexagonal mode appears first (for large G), the long-wavelength mode does not appear as a secondary instability. Since the time scale of formation of the hexagons is the vertical diffusion time ($d^2/\kappa \approx 0.1$ s), while the time scale for the long-wavelength mode is the horizontal diffusion time ($L^2/\kappa \approx 3$ hours), quickly ramping the temperature above $M = 80$ allows formation of the hexagons as the primary instability even when the long-wavelength instability would be primary if ΔT were increased quasi-statically, as assumed by linear theory. If ΔT is then decreased slowly below onset of hexagons, a dry spot can form once the hexagons have disappeared.

For small F and H, the transition depth d_t from dry spots to hexagons is predicted to be

$$d_t \approx \left(120\nu\kappa/g\right)^{1/3}. \tag{5.1}$$

(There is an H- and F-dependence but it is weak because of the cubic root.) In the 0.102 cm^2 s^{-1} silicone oil with air as the gas layer, we see the transition from long-wavelength to hexagons at $d_t = 0.024 \pm 0.001$ cm, close to the prediction of $d_t = 0.023 \pm 0.001$ cm. Using either a large F or helium in the gas layer shifts the long-wavelength/hexagon transition depth. The formation of the dry spot induces
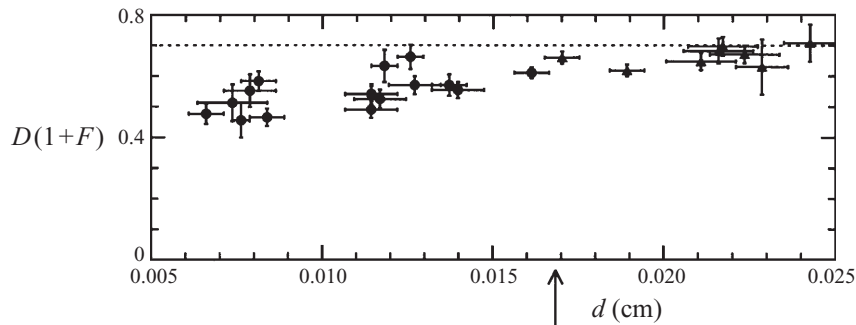
FIGURE 24. Experimental data for the onset of instability with increasing ΔT in 0.102 cm^2 s^{-1} silicone oil with an air gas layer and $F < 1/2$. The two-layer model prediction is given by the dashed line at $D(1 + F) = 0.70$. The transition from dry spots (circles) to dry spots with hexagons in the surrounding region (triangles) occurs around $d = 0.017$ cm (vertical arrow). Above $d = 0.024$ cm, hexagons are the primary instability.

hexagons in the elevated region of the cell for $d \geqslant 0.017$ cm. This transition depth is F-dependent since the change in the local vertical temperature difference is F-dependent (see (3.3)); in our experiments, $F = 0.3$–0.5 near the transition from dry spots to dry-spot-induced hexagons.

The steady-state deformation before onset of the instability blurs the distinction between dry-spot-induced hexagons and hexagons near d_t. For d slightly less than d_t, the hexagons form in part of the cell due to the steady-state deformation, but the liquid still becomes unstable to the dry spot. For d slightly above d_t, the hexagons fill the entire cell before the liquid can become unstable to the long-wavelength instability, but the interface is severely deformed.

6. Conclusions

Two modes of instability exist in surface-tension-driven Bénard–Marangoni convection where the liquid is heated from below and cooled from above. The short-wavelength hexagonal mode ($q = 1.99$) occurs for large G, when diffusion is the important (slow) stabilizing mechanism. The long-wavelength deformational mode ($q = 2\pi d/L \ll 1$) occurs for small G, when gravity is the important (slow) stabilizing mechanism. This long-wavelength instability can take the form of either a localized depression that evolves to a dry spot, or a localized elevation (high spot) that accelerates upwards and causes the liquid to pop up to the top plate. The relative thicknesses and thermal conductivities of the liquid and gas layers determine whether the dry spot or high spot forms: a high spot forms where the liquid thermal conductivity is much larger than the gas thermal conductivity and the liquid depth is nearly equal to or greater than the gas depth. The deformation due to the long-wavelength mode can cause the formation of the hexagonal mode by increasing the local value of M above the critical value for the hexagons.

The long-wavelength instability is described by an evolution equation for the height of the interface. Analysis of the evolution equation predicts that the instability is subcritical and that the unstable, backwards branch of the bifurcation curve never turns over to a stable branch. Numerical simulations of the evolution equation reveal states that agree qualitatively with states seen in the experiment.

Experimental study of the long-wavelength mode shows that a two-layer model is necessary to describe the onset of the deformational long-wavelength mode. The onset prediction of the two-layer model comes closer to the experimental measurements of onset than does the prediction of the one-layer model, although at thin liquid depths there is significant deviation between two-layer theory and experiment. For these thin liquid depths, the onset occurs earlier in experiment than predicted. In addition, the experiments exhibit steady-state deformation before onset of the instability. Both the premature onset and steady-state deformation are indications of non-uniformities in the experiment. Theoretical analysis of the influence of non-uniformity in heating shows that even small (1%) non-uniformities in the imposed temperature difference can cause large ($\sim 30\%$) deformations of the interface before the interface becomes unstable to the long-wavelength instability. Small non-uniformities in heating also cause the instability to occur at smaller temperature differences than predicted by theory, though this shift in onset is not as large as seen in the experiment. Non-uniformities due to the sidewall are the most likely culprit and we have begun a theoretical study of the effect of the sidewalls upon the formation of the long-wavelength instability.

Marangoni convection experiments aboard Apollo 14 (Grodzka & Bannister 1972) and Apollo 17 (Grodzka & Bannister 1975) yielded Bénard convection cells, and not the long-wavelength instability, even though $G < 1$. Several factors explain why the long-wavelength instability was not observed in the Apollo experiments. Fast ramping was used in the experiments since onset occurred at around 30 s – of order the vertical diffusion time (d^2/κ) – after initiation of the experiment; as mentioned in §5.4, fast ramping allows hexagons to form for smaller G than predicted by stability theory. More importantly, however, the long-wavelength onset condition in microgravity can differ greatly from the onset condition in terrestrial gravity. According to (3.15), the correction to the $q = 0$ onset condition for an experiment of finite size with fundamental physical wavenumber $q = 2\pi/L$ (rescaled wavenumber $q = 1$) is a factor of $(1 + 1/B)$; since $B \propto g$, in microgravity this correction factor becomes large and increases the long-wavelength onset in a finite-size cell by orders of magnitude. (In the Apollo experiments, the finite cell size correction shifted the onset of the long-wavelength mode to $M \sim 280$, above the onset of hexagons). In general, both surface tension and gravity stabilize the long-wavelength deformational instability. The static Bond number B characterizes the relative importances of these two stabilizing effects. When $L \gg d_{cap}$ ($B \gg 1$), where $d_{cap} = (\sigma/\rho g)^{1/2}$ is the capillary length, gravity plays the dominant stabilizing role and $D = 2G/3(1 + F)$ (with a small correction due to surface tension) is the onset condition. When $L \ll d_{cap}$ ($B \ll 1$), surface tension plays the dominant stabilizing role and $DB = 2/3(1 + F)$, or $MCr = \sigma_T \Delta T/\sigma = 2(2\pi d/L)^2/3(1 + F)$ (with a small correction due to gravity), is the onset condition. In our terrestrial experiments, $L = 26.5d_{cap}$ ($B = 18$) so surface tension plays no significant role. In microgravity experiments, $L \ll d_{cap}$ ($L \sim 0.06d_{cap}$ in the Apollo experiments) so surface tension plays the dominant stabilizing role for the long-wavelength instability; that is, the destabilization by thermocapillarity competes with the stabilization by surface tension, not gravity.

REFERENCES

BÉNARD, H. 1900 Les tourbillons cellulaires dans une nappe liquide. *Rev. Gén. Sci. Pure Appl.* **11**, 1261–1271, 1309–1328.

BERTOZZI, A. L., BRENNER, M. P., DUPONT, T. F. & KADANOFF, L. P. 1994 Singularities and similarities in interface flows. In *Trends and Perspectives in Applied Mathematics* (ed. L. Sirovich), pp. 155–208. Springer.

BLOCK, M. J. 1956 Surface tension as the cause of Bénard cells and surface deformation in a liquid film. *Nature* **178**, 650.

BURELBACH, J. P., BANKOFF, S. G. & DAVIS, S. H. 1990 Steady thermocapillary flows of thin liquid layers. II. Experiment. *Phys. Fluids* A **2**, 322–333.

CANUTO, C., HUSSAINI, M. Y., QUATERONI, A. & ZANG, T. A. 1987 *Spectral Methods in Fluid Dynamics*, p. 84. Springer.

CLOOT, A. & LEBON, G. 1984 A nonlinear stability analysis of the Bénard-Marangoni problem. *J. Fluid Mech.* **145**, 447–469.

CROSS, M. C. & HOHENBERG, P. C. 1993 Pattern formation outside of equilibrium. *Rev. Mod. Phys.* **65**, 851–1112.

DAVIS, S. H. 1983 Rupture of thin liquid films. In *Waves on Fluid Interfaces* (ed. R. E. Meyer), pp. 291–302. Academic.

DAVIS, S. H. 1987 Thermocapillary instabilities. *Ann. Rev. Fluid Mech.* **19**, 403–435.

DAVIS, S. H. & HOMSY, G. M. 1980 Energy stability theory for free-surface problems: buoyancy-thermocapillary layers. *J. Fluid Mech.* **98**, 527–553.

DEISSLER, R. J. & ORON, A. 1992 Stable localized patterns in thin liquid films. *Phys. Rev. Lett.* **68**, 2948–2951.

FUNADA, T. 1987 Nonlinear surface waves driven by the Marangoni instability in a heat transfer system. *J. Phys. Soc. Japan* **56**, 2031–2038.

GARCIA-YBARRA, P. L., CASTILLO, J. L. & VELARDE, M. G. 1987 A nonlinear evolution equation for Bénard-Marangoni convection with deformable boundary. *Phys. Lett.* A **122**, 107–110.

GOLDSTEIN, R. E., PESCI, A. I. & SHELLEY, M. J. 1995 Attracting manifold for a viscous topology transition. *Phys. Rev. Lett.* **75**, 3665–3668.

GOLOVIN, A. A., NEPOMNYASHCHY, A. A. & PISMEN, L. M. 1994 Interaction between short-scale Marangoni convection and long-scale deformational instability. *Phys. Fluids* **6**, 34–48.

GOLOVIN, A. A., NEPOMNYASHCHY, A. A. & PISMEN, L. M. 1997 Nonlinear evolution and secondary instabilities of Marangoni convection in a liquid-gas system with deformable interface. *J. Fluid Mech.* **341**, 317–341.

GOUSSIS, D. A. & KELLY, R. E. 1990 On the thermocapillary instabilities in a liquid layer heated from below. *Intl J. Heat Mass Transfer* **33**, 2237–2245.

GRODZKA, P. G. & BANNISTER, T. C. 1972 Heat flow and convection demonstration experiments aboard Apollo 14. *Science* **176**, 506–508.

GRODZKA, P. G. & BANNISTER, T. C. 1975 Heat flow and convection experiments aboard Apollo 17. *Science* **187**, 165–167.

HADJI, L., SAFAR, J. & SCHELL, M. 1991 Analytical results on the coupled Bénard-Marangoni problem consistent with experiment. *J. Non-Equilib. Thermodyn.* **16**, 343–356.

JOO, S. W., DAVIS, S. H. & BANKOFF, S. G. 1991 Long-wave instabilities of heated falling films. *J. Fluid Mech.* **230**, 117–146.

KOPBOSYNOV, B. K. & PUKHNACHEV, V. V. 1986 Thermocapillary flow in thin liquid films. *Fluid Mech. Sov. Res.* **15**, 95–106.

KOSCHMIEDER, E. L. & BIGGERSTAFF, M. I. 1986 Onset of surface-tension-driven Bénard convection. *J. Fluid Mech.* **167**, 49–64.

KRISHNAMOORTHY, S. & RAMASWAMY, B. 1995 Spontaneous rupture of thin liquid films due to thermocapillarity: A full-scale direct numerical simulation. *Phys. Fluids* **7**, 2291–2293.

NEPOMNYASHCHII, A. A. & SIMANOVSKII, I. B. 1990 Long-wave thermocapillary convection in layers with deformable interfaces. *Appl. Math. Mech.* **54**, 490–496.

NIELD, D. A. 1964 Surface tension and buoyancy effects in cellular convection. *J. Fluid Mech.* **19**, 341–352.

ORON, A. & ROSENAU, P. 1992 Formation of patterns induced by thermocapillarity and gravity. *J. Phys. II* (Paris) **2**, 131–146.

PANTALONI, J., BAILLEUX, R, SALAN, J. & VELARDE, M. G. 1979 Rayleigh-Benard-Marangoni instability: New experimental results. *J. Non-Equilib. Thermodyn.* **4**, 201–218.

PEARSON, J. R. A. 1958 On convection cells induced by surface tension. *J. Fluid Mech.* **4**, 489–500.

PÉREZ-GARCÍA, C. & CARNEIRO, G. 1991 Linear stability analysis of Bénard-Marangoni convection in fluids with a deformable free surface. *Phys. Fluids* A **3**, 292–298.

RASENAT, S., HARTUNG, G. WINKLER, B. L. & REHBERG, I. 1989 The shadowgraph method in convection experiments. *Exps. Fluids* **7**, 412-420.

SCANLON, J. W. & SEGEL, L. A. 1967 Finite amplitude cellular convection induced by surface tension. *J. Fluid Mech.* **30**, 149–162.

SCHATZ, M. F. & HOWDEN, K. 1995 Purification of silicone oils for fluid experiments. *Exps. Fluids* **19**, 359–361.

SCHATZ, M. F., VANHOOK, S. J., MCCORMICK, W. D., SWIFT, J. B. & SWINNEY, H. L. 1995 Onset of surface-tension-driven Bénard convection. *Phys. Rev. Lett.* **75**, 1938–1941.

SCRIVEN, L. E. & STERNLING, C. V. 1964 On cellular convection driven by surface-tension gradients: effects of mean surface tension and surface viscosity. *J. Fluid Mech.* **19**, 321–340.

SIVASHINSKY, G. I. 1982 Large cells in nonlinear Marangoni convection. *Physica* D **4**, 227–235.

SMITH, K. A. 1966 On convective instability induced by surface-tension gradients. *J. Fluid Mech.* **24**, 401–414.

TAKASHIMA, M. 1970 Surface-tension-driven convection with boundary slab of finite conductivity. *J. Phys. Soc. Japan* **29**, 531.

TAKASHIMA, M. 1981*a* Surface tension driven instability in a horizontal liquid layer with a deformable free surface. I. Stationary convection. *J. Phys. Soc. Japan* **50**, 2745–2750.

TAKASHIMA, M. 1981*b* Surface tension driven instability in a horizontal liquid layer with a deformable free surface. II. Overstability. *J. Phys. Soc. Japan* **50**, 2751–2756.

TAN, M. J., BANKOFF, S. G. & DAVIS, S. H. 1990 Steady thermocapillary flows of thin liquid layers. I. Theory. *Phys. Fluids* A **2**, 313–321.

VANHOOK, S. J, SCHATZ, M. F., MCCORMICK, W. D., SWIFT, J. B. & SWINNEY, H. L. 1995 Long-wavelength instability in surface-tension-driven Bénard convection. *Phys. Rev. Lett.* **75**, 4397–4400.

WILSON, S. K. 1993 The effect of a uniform magnetic field on the onset of steady Bénard-Marangoni convection in a layer of conducting fluid. *J. Engng Maths* **27**, 161–188.